Associative spine enlargement stabilizes wakefulness and enables goal-directed behaviors

Authors: Siqi Zhou[1,2†], Takeshi Sawada[1,2†], Tomoki Arima[1-3], Sadam Khan Panezai[1,2], Masanari Ohtsuka[1,2], Hitoshi Okazaki[1-3], Shunki Takaramoto[1,2], Shin-Ichiro Terada[1,3], Masashi Kondo[1,3], Takaaki Hashimoto[1,3], Kenichi Ohki[1,3], Masanori Matsuzaki[1,3,4,5], Sho Yagishita[1,2] & Haruo Kasai[1,2]*

Affiliations:
[1]International Research Center for Neurointelligence (WPI-IRCN), UTIAS, The University of Tokyo; Bunkyo-ku, Tokyo 113-0033, Japan.
[2]Laboratory of Structural Physiology, Center for Disease Biology and Integrative Medicine, Faculty of Medicine, The University of Tokyo; Bunkyo-ku, Tokyo 113-0033, Japan.
[3]Department of Physiology, Graduate School of Medicine, The University of Tokyo; Bunkyo-ku, Tokyo 113-0033, Japan.
[4]Brain Functional Dynamics Collaboration Laboratory, RIKEN Center for Brain Science, Saitama, 351-0198, Japan.
[5]Department of Biological Sciences, Graduate School of Science, The University of Tokyo, Tokyo, 113-0033, Japan.

*Corresponding author. hkasai@m.u-tokyo.ac.jp (H.K.)
[†]These authors contributed equally to this work.

Abstract

Models of cognition often treat fast electrical dynamics as separate from slower associative plasticity. We asked whether rapid synaptic structural plasticity is required for coordinated cortical processing during wakefulness. We developed SynC, a chemogenetic perturbation that, upon A/C administration, reversibly blocks associative dendritic spine enlargement and impairs motor learning without detectably altering baseline synaptic/neuronal physiology. SynC activation in frontoparietal cortex reduced laser-dot chasing and delayed feeding initiation, and reduced wake-state stability. Population recordings revealed a locomotor-active but impaired regime with preserved mean activity and γ power but reduced pairwise correlations during quiet, immobile epochs, with increased network dimensionality (Interm-C), intermittently interrupted by an arrest state (State-C) with suppressed γ power. Thus, intact Rac1-dependent spine-enlargement mechanisms are acutely required to maintain the functional coupling necessary for coordinated cortical processing during wakefulness.

One sentence summary: Acute, reversible in vivo blockade of associative spine enlargement shows that rapid structural plasticity is required to sustain cortical processing in EEG/EMG-defined waking.

Introduction

Electrophysiological waking, operationally defined by EEG/EMG, supports flexible sensorimotor integration and goal-directed behavior. Task-relevant cortical processing is expressed in ongoing patterns of population activity, yet maintaining these patterns over time requires mechanisms that preserve and update context (*1, 2*). Despite the centrality of memory-related mechanisms to awake cognition, the specific contribution of rapid associative synaptic plasticity to sustaining coordinated cortical processing and stable wakefulness remains unclear. Pharmacological manipulations have implicated NMDA receptor–dependent processes in learning and cognition; for example, NMDA receptor antagonists such as ketamine disrupt associative plasticity and impair cognitive performance (*3*) and can induce anesthesia (*4*), but they also broadly suppress NMDA receptor–mediated synaptic currents, and accompany excitatory periods before sedation. Thus, the specific role of rapid plasticity mechanisms—distinct from general synaptic transmission—in sustaining wakefulness and task-relevant cortical processing remains elusive.

A major obstacle is that many candidate microstructural processes act on spatial and temporal scales that are difficult to observe directly during behavior. Most excitatory synapses reside on actin-rich dendritic spines, which can undergo a rapid increase in head volume that persists for minutes or longer following coincident pre- and postsynaptic activity (*5-7*); we refer to this coincidence-gated structural change as associative spine enlargement. Spine enlargement can strengthen synaptic connections via at least two routes: (i) AMPA receptor recruitment and stabilization, as studied in long-term potentiation (LTP) (*6, 8-10*); and (ii) a potential trans-synaptic mechanotransduction route, in which actin-driven expansion engages adhesion complexes and could influence presynaptic release (*7, 10, 11*). The onset of associative plasticity may occur within seconds (*12, 13*), yet sub-minute in vivo measurements during goal-directed behavior remain technically challenging. A major challenge in awake animals is that transient, coordinated structural changes associated with learning can be masked by ongoing non-associative spine dynamics and baseline fluctuations (*14, 15*).

To overcome this obstacle, we tested whether associative spine enlargement is necessary using an acute, reversible postsynaptic perturbation in vivo, rather than requiring direct visualization of sub-minute events. This strategy distinguishes a spine-localized mechanism from global state changes by preserving baseline physiology and showing rapid reversibility. Accordingly, we developed SYNCit-C (SynC), a

chemogenetic variant of SYNCit-K (SynK) (*16*), that selectively and transiently abolishes dendritic spine enlargement upon administration of the A/C heterodimerizer, without measurably affecting basal synaptic transmission, NMDA receptor–mediated slow EPSCs, or intrinsic membrane properties. We expressed SynC broadly across the frontoparietal cortex to test whether spine enlargement contributes to coordinated cortical processing during wakefulness (*17*). A/C administration induced severe deficits in awake behaviors and produced an intermittent non-arousal arrest state (State-C), distinct from slow-wave sleep (SWS) and characterized by behavioral arrest with a specific EEG signature. Together, these findings support the view that associative spine-enlargement is not only engaged during learning and memory but is also required to sustain coordinated cortical processing and stabilize wakefulness.

Selective inhibition of spine enlargement by SynC

We designed SynC to block activity-dependent spine enlargement, building on the previously reported SynK system, which uses a rapamycin derivative (A/C) to induce heterodimerization of FKBP (FK506-binding protein) and FRB (the FKBP12–rapamycin binding domain of mTOR) (Fig. 1A) (*16*). Because SynK implicated Rac1 activation by Rac1-GEFs in spine enlargement (Fig. 1B), we generated SynC in which both components were expressed from the CaMKII promoter: a PSD-anchored PSDΔ1,2–FRB and a cytosolic FKBP–Rac1-GAP (the GAP domain of α1-chimaerin) to inactivate Rac1 by GTP hydrolysis (Fig. 1C). PSDΔ1,2–FRB–mVenus localized selectively to postsynaptic densities and was absent from axons (fig. S1A,B).

We first confirm that SynC–A/C spares baseline physiology and global excitability in slice and dissociated culture, and then test the time course and reversibility in vivo. Application of A/C rapidly recruited the FKBP fusion from dendritic shafts into spines (fig. S1C–F and S2A) and abolished rapid spine enlargement evoked either by two-photon glutamate uncaging in 0 Mg^{2+} ACSF (Fig. 1E; exact statistics in fig. S2B) (*7*) or by a chemical LTP (cLTP) protocol (Fig. 1F and fig. S1C–F), an effect not observed with the GAP-dead mutant SynC-dGAP (Fig. 1E and fig. S1C–F). These results are consistent with rapid Rac1-GAP catalysis being sufficient to suppress Rac1-dependent spine enlargement under these conditions (*18, 19*).

Basal excitatory and inhibitory synaptic transmission and intrinsic membrane properties were unchanged, and NMDA receptor–mediated slow EPSCs were unaffected (fig. S2C-G), consistent with stable somatic and spine Ca^{2+} signals in vivo (fig. S9A,B).

For most subsequent experiments, we used a bicistronic plasmid in which the

126 FRB and FKBP modules of SynC were co-expressed via an internal ribosome entry site
127 (IRES), enabling single-vector AAV-mediated delivery for in vivo use (fig. S3A) (*16*).
128 Importantly, we found that the A/C-induced suppression of spine enlargement was
129 transient, dissipating within ~1 h at the low expression levels used in subsequent
130 experiments (Fig. 1F and fig. S3A–C). This rapid loss of efficacy was unexpected
131 because FKBP–mVenus fluorescence persisted (fig. S3C) and may reflect inactivation
132 of the tethered Rac1-GAP (*20*). This transient efficacy provides a key experimental
133 advantage: cortical phenotypes are rapidly reversible in vivo (see Fig. 4G). SynC did
134 not alter NMDA-evoked spine shrinkage (fig. S3D), nor baseline spine morphology or
135 intrinsic spine volume dynamics (Fig. 1G and fig. S3E)(*14, 16*), consistent with
136 preserved basal actin-dependent processes. For in vivo AAV delivery, mVenus was
137 replaced by an HA tag, reducing the expression cassette to 4.5 kb (Fig. 2A).
138

139 **Local SynC expression in primary visual and motor cortices**

140 We tested whether SynC perturbs basic response properties in primary visual cortex
141 (V1). SynC was delivered to Thy1–GCaMP6s transgenic mice by AAV (1.2×10^{13} gc
142 mL^{-1}; 1 μL; fig. S4A,B). Four weeks later, we recorded grating-evoked responses from
143 hundreds of neurons. A/C (2 mg kg^{-1}) was then administered intraperitoneally (i.p.)
144 under light anesthesia (Methods). Retinotopy, orientation selectivity, and neuronal
145 firing rates were unchanged after A/C in SynC-expressing mice (SynC@V1) (fig. S4C–
146 K). Thus, acute SynC activation did not impair basic visual processing in V1, indicating
147 that intrinsic membrane properties and synaptic transmission remained intact in vivo,
148 consistent with in vitro controls.
149 We next examined motor learning in primary motor cortex (M1). SynC was
150 bilaterally delivered to the forelimb representation by AAV (Fig. 2A), and rotarod
151 training was performed 4 weeks later. Within 30 min of i.p. A/C, translocation of HA–
152 FKBP–Rac1-GAP to dendritic spines was detected in fixed SynC@M1 tissue (Fig. 2B).
153 In controls, performance improved rapidly within the first 20 min, typically plateaued
154 by ~30 min, and was maintained on the next day (Fig. 2C and D). In SynC@M1 mice,
155 A/C abolished rotarod learning, whereas A/C alone or A/C in SynC-dGAP mice left
156 learning and consolidation intact (Fig. 2D). These data indicate that motor learning in
157 this task requires Rac1-dependent spine enlargement, which SynC–A/C blocks via
158 inhibition of Rac1 at spines.
159

160 **SynC expression across frontoparietal cortex**

161 To test the impact of spine enlargement on goal-directed behavior (*17*), we bilaterally

162 transduced SynC using AAV (1.2×10^{13} gc mL^{-1}; 4 μL) in neonatal pups (P1) under
163 hypothermic anesthesia, targeting a site between S1 and M2 in the sagittal plane (AP, 0
164 to 1 mm; ML, 1 mm) (Fig. 3A; fig. S5A,B). Injection at P1 ensured extensive cortical
165 distribution (*21*). At 6 to 12 weeks post-injection, histology showed broad expression
166 spanning from prefrontal cortex (M2) to posterior parietal cortex (PPC), with minimal
167 subcortical labeling except for minor dorsal striatal spillover (fig. S5C). Across
168 transduced areas, 20 to 80% of $NeuN^+$ layer 5 neurons expressed SynC, varying by
169 cortical region (fig. S5C). No gross or cytoarchitectural abnormalities were detected
170 (Fig. 3A), and SynC@FPC mice displayed normal motor performance in the rotarod
171 task comparable to WT mice (Fig. 2E). The cortical thickness of middle sagittal sections
172 was ~8% smaller in SynC@FPC mice than in SynC-dGAP@FPC mice, but this
173 difference was not significant (Methods). Expression was most prominent in layer V
174 neurons, moderate in layers II/III, and nearly absent in layer VI, consistent with the
175 CaMKII promoter (Fig. 3A; fig. S5D). PSDΔ1,2–FRB–mVenus was largely restricted
176 to dendritic spines, with no clear labeling in dendritic shafts, somatic cytosol, nucleus,
177 or axons in vivo (fig. S5E).
178 Following i.p. A/C, SynC@FPC mice showed profound impairments in goal-
179 directed behavior (Fig. 3B–D). In the open field, center exploration was reduced more
180 strongly in SynC@FPC than in SynC@M1 mice, despite similar changes in locomotor
181 speed (Fig. 3B). In a laser-dot chasing assay (Methods), pursuit dropped from 80% pre–
182 A/C to 15% post–A/C (n = 26 SynC@FPC; Fig. 3C; Movies S1 to S4), whereas SynC-
183 dGAP@FPC controls were unaffected (n = 11; Fig. 3B,C). In a food-pellet task, feeding
184 initiation latency increased from ~30 s to ~150 s after A/C despite frequent encounters
185 with the pellet (Fig. 3D; Movies S5 to S7), indicating impaired initiation of goal-
186 directed actions while basic motor output and consummatory behavior remained intact.
187 To quantify onset and recovery, we analyzed a separate dark-phase cohort (see Fig. 4G).
188

189 **Intermittence of State-C and Interm-C**

190 Following i.p. injection of A/C in the open-field arena, 41 of 57 SynC@FPC mice
191 exhibited intermittent behavioral arrests beginning 5 to 15 min post-injection (Fig. 4A).
192 These arrests cumulatively occupied ~31.2% (± 3.8%) of the first hour. Arrest episodes
193 frequently occurred during standing at the end of running bouts ("standing"), while
194 navigating corners ("corner"), or during grooming ("grooming") (fig. S6; Movies S8 to
195 S11). During these episodes, animals remained motionless in an low-arousal arrest state
196 with eyes open, head elevated, and tail extended, typically fully standing or partially

197 seated ("corner"), except for occasional minor postural shifting in the "corner" state
198 (fig. S6B; see below).
199 To relate phenotype to SynC expression levels, we performed whole-brain
200 histology in 21 mice. The five mice without State-C showed <20% neuronal expression,
201 whereas State-C reliably appeared when expression exceeded this threshold (Fig. 4B;
202 fig. S5C). Because the occurrence of State-C reliably indicated sufficient SynC
203 expression, behavioral assays shown in Fig. 3C,D were analyzed specifically in mice
204 exhibiting State-C to ensure phenotype–expression consistency. State-C required Rac1-
205 GAP activity in neocortical dendritic spines, as A/C did not induce State-C in SynC-
206 dGAP@FPC mice with histologically confirmed expression (Fig. 4E; fig. S5B,C).
207 Expression of the FKBP–Rac1-GAP–HA component alone also failed to induce State-C
208 (Fig. 4E), arguing against confounding effects mediated by endogenous mTOR
209 signaling. Local SynC expression in M1 never caused State-C (Fig. 4E).
210 Electrophysiologically, State-C was characterized by reduced EMG tone and
211 suppressed γ-band power, reminiscent of SWS (Fig. 4C,D; fig. S7A–C). Unlike typical
212 SWS, State-C did not exhibit a robust increase in slow-wave (δ-band) power (Fig.
213 4C,D; fig. S7C). This contrasts with the robust slow-wave increase previously reported
214 for SynK, which promotes spine enlargement in frontal cortex (*16*). Isolated sleep
215 spindles, a hallmark of stage-2 sleep, were frequently observed in State-C but rarely
216 seen in matched control recordings (fig. S7A) (*22*). Spike-and-wave discharges
217 characteristic of absence seizures (*23*) were not observed (Movie S8). Pupils constricted
218 (miosis), heart rate modestly decreased, and respiration remained unchanged, similar to
219 autonomic patterns observed in SWS (Fig. 4F). However, this autonomic/motor
220 signature clearly differed from arrest induced by fear or brainstem stimulation (*24*).
221 REM sleep (θ-band dominance with low EMG; fig. S7A) was not observed during
222 State-C, distinguishing it from narcolepsy (*25*). For differential classification from
223 sleep, seizure, anesthesia, and related arrest states, see Table S1.
224 A/C intermittently caused State-C. EEG γ-band power (30 to 80 Hz) in Interm-C
225 remained comparable to awake periods recorded from the same mice prior to A/C
226 administration (awake baseline) (Fig. 4C,D; fig. S7C). The duration of Interm-C bouts
227 followed a heavy-tailed distribution, similar to awake bouts in WT mice, whereas State-
228 C bout durations were exponentially distributed (fig. S7D). Interm-C and State-C thus
229 alternated finely (Fig. 4D), with State-C episodes often briefly interrupted (0.5 to 10 s)
230 by short movements ("shifting") that coincided with transient EEG γ activation,
231 especially during "corner" postures (fig. S6B; Movie S12). These alternating dynamics

resemble sleep–wake transitions and suggest flip-flop-like mechanisms mediated by the ascending reticular activating system (ARAS) (*25, 26*).

To examine the time course during stable wakefulness, we housed mice on an inverted light–dark cycle and tested them during their nocturnal (active) phase. State-C emerged similarly to tests performed during the normal inactive (light) phase (31% ± 4.6%, n = 49). The onset of State-C and impairments in laser chasing and food-pellet tasks occurred by ~10 min after A/C administration and resolved by ~60 min (Fig. 4G). This reversibility paralleled the transient SynC–A/C action on spine enlargement observed in dissociated culture (fig. S3B). Occurrence of State-C, impaired laser chasing, and delayed feeding initiation resolved in parallel (Fig. 4G), supporting a common mechanism—acute inhibition of spine enlargement. The transient nature of SynC–A/C effects was further confirmed by normal rotarod performance tested one day after training, even when A/C administration shortly after training had induced State-C (Fig. 2E), indicating that newly acquired motor memories were preserved and consolidated. Moreover, A/C-induced State-C was reproducible three weeks later in 8 of 9 previously responsive mice (Fig. 4E), demonstrating that transient SynC–A/C action does not induce long-lasting neural dysfunction or tolerance.

The impairment is unlikely to reflect generalized cortical suppression or A/C alone: during impaired but locomotor-active periods (Interm-C), EEG γ-band power remained comparable to awake baseline (Fig. 4C,D), and A/C alone did not induce Interm-C/State-C. Orthogonal controls (including the catalytically inactive SynC-dGAP and the mislocalized FKBP–Rac1-GAP alone control; Fig. 4E) further constrain alternative explanations tied to expression or dimerization per se.

Transitions between Interm-C and State-C

Transitions into State-C occurred during both the light and dark phases (Fig. 4E,G). Entry into State-C was observed even in the dark (active) phase, when mice are normally awake (Fig. 4G), and the probability of transition was similar across phases (Fig. 4E,G). This phase-independence argues against a purely circadian or sleep-drive explanation and suggests that, under widespread cortical SynC activation, arousal can intermittently become unstable. To characterize the temporal structure of these transitions, we performed time-resolved analyses of Interm-C→State-C transitions (Fig. 4D; fig. S8; see Fig. 4H for operational definitions). In untreated control mice, spontaneous sleep onset proceeded gradually, with progressive declines in locomotor velocity, EMG tone, and cortical γ-band power over 10 to 60 s (fig. S8A; Movie S13). In contrast, SynC@FPC mice after A/C exhibited abrupt transitions, marked by rapid

268 decreases in locomotor velocity and cortical γ-band power within ~10 s (fig. S8B,C;
269 Movie S14). Time-locked averages revealed highly reproducible transition profiles
270 across animals (fig. S8). Despite variability in awake behavior, this stereotyped pattern
271 is consistent with a model in which cortical associative activity helps stabilize arousal
272 (potentially via subcortical arousal systems) and buffers against sudden inactivation;
273 when cortical control is disrupted, rapid inactivation can produce immediate behavioral
274 arrest (State-C) even during ongoing movement.
275 Across three goal-directed behavioral assays—open-field center exploration
276 (motivation), laser-dot chasing (attention/motivation), and feeding initiation
277 (motivation)—SynC–A/C consistently impaired performance. These assays likely
278 engage multiple processes (e.g., perception, attention, motivation) and were not
279 designed to isolate specific domains; we therefore interpret them collectively as an
280 integrated capacity for goal-directed cortical processing. Because State-C occurred
281 frequently and Interm-C episodes were temporally fragmented, tasks requiring sustained
282 engagement (e.g., T-maze, novel object recognition) could not be performed or
283 interpreted reliably under these conditions. In this study, our aim was to establish that
284 rapid dendritic-spine enlargement is required for intact goal-directed cortical
285 performance and for stabilization of wakefulness.
286
287 **Ca^{2+} imaging from primary motor cortex (M1)**
288 We performed two-photon Ca^{2+} imaging in the forelimb area of M1 in head-fixed
289 SynC@FPC mice co-expressing GCaMP7f while the mice ran on a treadmill (Fig.
290 5A,B). The amplitudes and time courses of Ca^{2+} transients were unchanged following
291 A/C administration (Fig. 5C; fig. S9A,B), indicating that SynC–A/C did not measurably
292 alter the fast Ca^{2+} signals used here and supporting intact voltage-gated conductances
293 and NMDA receptor function (*27*), consistent with in vitro controls (fig. S2C-F) and V1
294 recordings (fig. S4). Mice typically ran at mean velocities of 4.7 ± 1.5 cm s^{-1} (mean ±
295 s.e.m., n = 5 mice) during the Awake (immobile) and 3.5 ± 1.3 cm s^{-1} during Interm-C.
296 During ~30% of the recorded time, mice stopped moving and became immobile (Fig.
297 5D). When immobile, Awake mice maintained a stable posture with their legs
298 positioned to grasp the treadmill, whereas during Interm-C leg positions were more
299 variable and poorly controlled (Movies S15 and S16).
300 The immobile epochs enabled analysis of cortical activity independent of
301 movement. Firing rates were not significantly reduced after A/C administration during
302 Interm-C (Fig. 5E), consistent with preserved γ-band power in Interm-C (fig. S7C). By
303 contrast, pairwise correlations during immobile Interm-C epochs were reduced after

A/C (Fig. 5F,G). Concurrently, network dimensionality increased, as indicated by an increased number of principal components explaining 50% of the variance (D50) and an increased participation ratio (PR) (fig. S9C,D). This combination—reduced correlation with increased dimensionality—supports weakened functional coupling among M1 neurons rather than generalized suppression of firing. Correlation structure partially recovered ~1 h after A/C, particularly during immobile epochs (Fig. 5F). These changes coincide with impaired goal-directed behavior during Interm-C and are consistent with inhibition of associative plasticity by SynC. The dissociation between correlation structure and firing rate is consistent with prior electrophysiological findings showing perception-related membrane depolarization without proportional spike-rate modulation (*28*). Because pairwise correlations are estimated over finite windows, strengthened coupling can translate into coordination that builds with variable latency rather than instantaneously.

When State-C was identified in treadmill sessions based on EEG and EMG power (Fig. 5D), firing rates were reduced to levels comparable to SWS. However, pairwise correlations remained reduced and dimensionality remained elevated in State-C—contrasting with SWS, where correlations typically increase and dimensionality decreases due to slow-wave synchrony (*28*). Consistently, slow-wave synchrony was suppressed during State-C. A compact cross-state summary of behavioral and neural signatures is provided in Table S2.

Discussion

We developed SynC, a chemogenetic tool acutely activated by the A/C heterodimerizer, which reversibly suppresses associative spine enlargement while sparing basal actin-dependent spine dynamics (Fig. 1G). These features, together with multiple physiological and genetic controls, make nonspecific off-target explanations less likely. SynC–A/C also spared neurophysiology, including NMDA receptor–mediated responses (fig. S2C–G and S9A,B). Consistent with this, we observed no seizure-like activity or epileptiform discharges, unlike conditions in which NMDAR is blocked (*29*). In vivo, cortical SynC–A/C left early visual responses in V1 intact (fig. S4) but impaired long-term motor learning assessed by rotarod performance (Fig. 2). With broad expression across the frontoparietal cortex, SynC–A/C rapidly disrupted goal-directed behaviors during wakefulness (Interm-C), including open-field exploration, laser-dot chasing, and feeding initiation, and mice intermittently entered a distinct arrest-like, low arousal state (State-C) with a specific EEG/EMG signature (Fig. 4;

Table S1). SynC expression alone produced no detectable baseline effects before A/C administration. Both Interm-C and State-C showed rapid onset (~5 min) and reversal (~60 min) following A/C administration (Fig. 4G), consistent with the in vitro kinetics of SynC blockade of spine enlargement (Fig. 1F; fig. S3B).

To assess target specificity, we combined subcellular localization, genetic controls, and physiological measurements. The PSD-anchored FRB module localized to postsynaptic densities. Critically, the GAP-dead control (SynC-dGAP) preserved FRB/FKBP scaffolding and A/C-driven recruitment but eliminated Rac1-GAP catalysis and produced no rapid behavioral (Fig. 3) or electrophysiological phenotypes (fig. S2C–G), arguing against ligand- or scaffold-driven explanations. Rapid reversibility serves as a built-in rescue, arguing against irreversible damage or slow adaptive changes, and is difficult to reconcile with slower, global downstream consequences of Rac1 perturbation—for example redox-linked stress signaling and ROS-dependent activation of JNK—which would not be expected to track the minute-scale on/off kinetics (*18, 19*). Finally, the behavioral and EEG/EMG signatures of Interm-C/State-C differ from anesthesia, absence-like seizures, and cataplexy: Interm-C preserved gamma power and mean spiking, whereas State-C suppressed gamma power without a strong delta increase (Table S1). Together, these constraints make a nonspecific off-target explanation unlikely.

SynC–A/C also attenuated the rise in slow-wave activity (SWA), whereas promoting spine enlargement with SynK–A/C (a Rac1-GEF probe) increased SWA (*16*). These opposite effects support the view that the dominant action of SynC is blockade of spine enlargement. The complementary effects on arousal further suggest a top-down cortical influence on brainstem systems. Both manipulations reduce indices of cortical processing—SynC by blocking associative plasticity and inducing ensemble decorrelation (expanded dimensionality), and SynK by promoting slow-wave bistability that synchronizes up–down transitions and interrupts information exchange—yet both reduce arousal. Such top-down modulation of sleep has been proposed in psychological (*30*) and physiological frameworks (*16, 31, 32*) and is anatomically plausible given frontal-cortex projections to brainstem nuclei (*33, 34*), although the specific targets remain unidentified and beyond the scope of this study.

Modern systems neuroscience often summarizes mean firing rate or overall population activity as a proxy for "cognitive engagement." However, goal-directed cognition requires the moment-to-moment retention and updating of context that links perception to action, which may be supported by transient synapse- and plasticity-dependent network states rather than static firing levels alone (*35, 36*). Consistent with

this, acute suppression of associative plasticity—specifically spine enlargement—impaired goal-directed performance and destabilized wakefulness even when mean population activity and γ power were preserved during Interm-C, pointing to a requirement for rapid, state-dependent updating of effective circuit coupling beyond firing-rate–centric summaries.

Although the precise kinetics of cortical associative plasticity remain uncertain, multiple lines of evidence indicate that key components occur rapidly (*12, 13, 37, 38*). Increases in postsynaptic glutamate sensitivity, however, can require longer (~2 min) (*9, 39*), suggesting that the earliest functional consequences of associative plasticity may involve additional fast components. These could include trans-synaptic mechanical effects of spine enlargement on presynaptic terminals (*7, 11*), consistent with prior reports of presynaptic expression of associative plasticity in neocortex (*40-42*). Current in vivo spine-volume estimates are diffraction-limited and, in awake cortex, are further challenged by motion artifacts (*10, 43-45*) and intrinsic spine dynamics (Fig. 1G) (*14, 15, 46*). Even time-locked induction strategies intended to boost detectability remain technically demanding and low-yield in awake animals (*13, 38*). Moreover, coordinated synaptic changes as small as 1–2% can be functionally significant (*47*), yet intrinsic spine dynamics are often an order of magnitude larger, making learning-locked sub-minute events difficult to identify.

Future advances that resolve task-locked spine dynamics in vivo will clarify the temporal precision and input requirements of rapid associative plasticity. By enabling acute, reversible blockade of associative spine enlargement while sparing baseline physiology, SynC provides a mechanistic bridge between a synaptic plasticity step and coordinated cortical processing during wakefulness, a dependence not captured by firing rate alone.

References and notes

1. A. Baddeley, The episodic buffer: a new component of working memory? *Trends in cognitive sciences* **4**, 417–423 (2000).
2. J. Jonides *et al.*, The mind and brain of short-term memory. *Annu Rev Psychol* **59**, 193–224 (2008).
3. N. R. Driesen *et al.*, The impact of NMDA receptor blockade on human working memory-related prefrontal function and connectivity. *Neuropsychopharmacology* **38**, 2613–2622 (2013).
4. N. P. Franks, General anaesthesia: from molecular targets to neuronal pathways of sleep and arousal. *Nature reviews. Neuroscience* **9**, 370–386 (2008).
5. M. Matsuzaki, N. Honkura, G. C. Ellis-Davies, H. Kasai, Structural basis of long-term potentiation in single dendritic spines. *Nature* **429**, 761–766 (2004).
6. A. Holtmaat, K. Svoboda, Experience-dependent structural synaptic plasticity in the mammalian brain. *Nature reviews. Neuroscience* **10**, 647–658 (2009).
7. H. Kasai, H. Ucar, Y. Morimoto, F. Eto, H. Okazaki, Mechanical transmission at spine synapses: Short-term potentiation and working memory. *Curr Opin Neurobiol* **80**, 102706 (2023).
8. B. E. Herring, R. A. Nicoll, Long-term potentiation: from CaMKII to AMPA receptor trafficking. *Annu Rev Physiol* **78**, 351–365 (2016).
9. A. M. Getz *et al.*, High-resolution imaging and manipulation of endogenous AMPA receptor surface mobility during synaptic plasticity and learning. *Sci Adv* **8**, eabm5298 (2022).
10. K. M. Harris, M. Kuwajima, J. C. Flores, K. Zito, Synapse-specific structural plasticity that protects and refines local circuits during LTP and LTD. *Philos Trans R Soc Lond B Biol Sci* **379**, 20230224 (2024).
11. H. Ucar *et al.*, Mechanical actions of dendritic-spine enlargement on presynaptic exocytosis. *Nature* **600**, 686–689 (2021).
12. B. Gustafsson, F. Asztely, E. Hanse, H. Wigstrom, Onset Characteristics of Long-Term Potentiation in the Guinea-Pig Hippocampal CA1 Region in Vitro. *Eur J Neurosci* **1**, 382–394 (1989).
13. S. El-Boustani *et al.*, Locally coordinated synaptic plasticity of visual cortex neurons in vivo. *Science* **360**, 1349–1354 (2018).
14. H. Kasai, N. E. Ziv, H. Okazaki, S. Yagishita, T. Toyoizumi, Spine dynamics in the brain, mental disorders and artificial neural networks. *Nature reviews.*

Neuroscience **22**, 407–422 (2021).

15. G. Mongillo, S. Rumpel, Y. Loewenstein, Intrinsic volatility of synaptic connections — a challenge to the synaptic trace theory of memory. *Current Opinion in Neurobiology* **46**, 7–13 (2017).
16. T. Sawada *et al.*, Prefrontal synaptic regulation of homeostatic sleep pressure revealed through synaptic chemogenetics. *Science* **385**, 1459–1465 (2024).
17. L. International Brain *et al.*, A brain-wide map of neural activity during complex behaviour. *Nature* **645**, 177–191 (2025).
18. E. E. Bosco, J. C. Mulloy, Y. Zheng, Rac1 GTPase: a "Rac" of all trades. *Cellular and molecular life sciences : CMLS* **66**, 370–374 (2009).
19. N. Arimura, K. Kaibuchi, Neuronal polarity: from extracellular signals to intracellular mechanisms. *Nature reviews. Neuroscience* **8**, 194–205 (2007).
20. E. M. Griner *et al.*, A novel cross-talk in diacylglycerol signaling: the Rac-GAP beta2-chimaerin is negatively regulated by protein kinase Cdelta-mediated phosphorylation. *J Biol Chem* **285**, 16931–16941 (2010).
21. C. E. Cheetham, B. D. Grier, L. Belluscio, Bulk regional viral injection in neonatal mice enables structural and functional interrogation of defined neuronal populations throughout targeted brain areas. *Frontiers in neural circuits* **9**, 72 (2015).
22. L. M. J. Fernandez, A. Luthi, Sleep Spindles: Mechanisms and Functions. *Physiol Rev* **100**, 805–868 (2020).
23. O. C. Snead, 3rd, Pharmacological models of generalized absence seizures in rodents. *J Neural Transm Suppl* **35**, 7–19 (1992).
24. H. Goni-Erro, R. Selvan, V. Caggiano, R. Leiras, O. Kiehn, Pedunculopontine Chx10(+) neurons control global motor arrest in mice. *Nat Neurosci* **26**, 1516–1528 (2023).
25. R. E. Brown, R. Basheer, J. T. McKenna, R. E. Strecker, R. W. McCarley, Control of sleep and wakefulness. *Physiol Rev* **92**, 1087–1187 (2012).
26. T. E. Scammell, E. Arrigoni, J. O. Lipton, Neural Circuitry of Wakefulness and Sleep. *Neuron* **93**, 747–765 (2017).
27. X. Chen, U. Leischner, N. L. Rochefort, I. Nelken, A. Konnerth, Functional mapping of single spines in cortical neurons in vivo. *Nature* **475**, 501–505 (2011).
28. T. A. Engel, N. A. Steinmetz, New perspectives on dimensionality and variability from large-scale cortical dynamics. *Curr Opin Neurobiol* **58**, 181–190 (2019).

29. F. R. Sharp, R. L. Hendren, Psychosis: atypical limbic epilepsy versus limbic hyperexcitability with onset at puberty? *Epilepsy & behavior : E&B* **10**, 515–520 (2007).
30. A. Lemyre, F. Belzile, M. Landry, C. H. Bastien, L. P. Beaudoin, Pre-sleep cognitive activity in adults: A systematic review. *Sleep Med Rev* **50**, 101253 (2020).
31. L. B. Krone *et al.*, A role for the cortex in sleep-wake regulation. *Nat Neurosci* **24**, 1210–1215 (2021).
32. K. Tossell *et al.*, Somatostatin neurons in prefrontal cortex initiate sleep-preparatory behavior and sleep via the preoptic and lateral hypothalamus. *Nat Neurosci* **26**, 1805–1819 (2023).
33. P. L. Gabbott, T. A. Warner, P. R. Jays, P. Salway, S. J. Busby, Prefrontal cortex in the rat: projections to subcortical autonomic, motor, and limbic centers. *J Comp Neurol* **492**, 145–177 (2005).
34. J. P. Do *et al.*, Cell type-specific long-range connections of basal forebrain circuit. *eLife* **5**, (2016).
35. D. G. Clark, L. F. Abbott, Theory of Coupled Neuronal-Synaptic Dynamics. *Physical Review X* **14**, (2024).
36. A. Lansner, F. Fiebig, P. Herman, Fast Hebbian plasticity and working memory. *Curr Opin Neurobiol* **83**, 102809 (2023).
37. M. A. Erickson, L. A. Maramara, J. Lisman, A single brief burst induces GluR1-dependent associative short-term potentiation: a potential mechanism for short-term memory. *J Cogn Neurosci* **22**, 2530–2540 (2010).
38. J. Noguchi *et al.*, Bidirectional in vivo structural dendritic spine plasticity revealed by two-photon glutamate uncaging in the mouse neocortex. *Scientific reports* **9**, 13922 (2019).
39. R. Yasuda, Y. Hayashi, J. W. Hell, CaMKII: a central molecular organizer of synaptic plasticity, learning and memory. *Nature reviews. Neuroscience* **23**, 666–682 (2022).
40. M. Volgushev, L. L. Voronin, M. Chistiakova, W. Singer, Relations between long-term synaptic modifications and paired-pulse interactions in the rat neocortex. *Eur J Neurosci* **9**, 1656–1665 (1997).
41. D. V. Buonomano, Distinct functional types of associative long-term potentiation in neocortical and hippocampal pyramidal neurons. *J Neurosci* **19**, 6748–6754 (1999).
42. I. Weichard *et al.*, Fully-primed slowly-recovering vesicles mediate presynaptic

LTP at neocortical neurons. *Proc Natl Acad Sci U S A* **120**, e2305460120 (2023).

43. M. Fu, X. Yu, J. Lu, Y. Zuo, Repetitive motor learning induces coordinated formation of clustered dendritic spines in vivo. *Nature* **483**, 92–95 (2012).

44. J. Cichon, W. B. Gan, Branch-specific dendritic Ca(2+) spikes cause persistent synaptic plasticity. *Nature* **520**, 180–185 (2015).

45. W. J. Wright, N. G. Hedrick, T. Komiyama, Distinct synaptic plasticity rules operate across dendritic compartments in vivo during learning. *Science* **388**, 322–328 (2025).

46. K. Ishii *et al.*, In Vivo Volume Dynamics of Dendritic Spines in the Neocortex of Wild-Type and Fmr1 KO Mice. *eNeuro* **5**, ENEURO.0282–0218.2018 (2018).

47. B. Feulner *et al.*, Small, correlated changes in synaptic connectivity may facilitate rapid motor learning. *Nature communications* **13**, 5163 (2022).

Acknowledgements

We thank S. Fujii, C. Fujinami, and Y. Hama for technical assistance, Xu, K. Aihara, T. R. Hira, T. Toyoizumi, K. Yoshida, Y. A. Iriki, T. Yamamori, Y. Hayashi, M. Kashiwagi, N. Kitajima, N. Matsumoto and M. Miyano for helpful discussions. During manuscript preparation, the authors used OpenAI's GPT-5 language model for English editing and phrasing refinement under full author supervision.

Funding: This work was supported by Brain/MINDS 2 (JP24wm0625101 to H.K., S.Z., T.S., S.T., T.H., and T.Y.; JP23wm0625001 to M.M, K.O., S.Y. and JP24wm0625308 to S.Y.; JP24wm0625203 to K.O. and T.H.) from AMED, CREST (JPMJCR21E2 to H.K.; JPMJCR22P1 to K.O.) and FOREST (JPMJFR231T to T.S.) from JST, KAKENHI (JP20H05685 to H.K., S.Z., T.S., and S.Y.; JP23K14385 to T.S.; JP23K14284 to S.T.; JP21H05176 and JP24K02115 to S.Y.; JP21K15612 and JP24K10472 to M.K.; JP22H05160 and JP23H00388 to M.M.; JP25K18580 to T.H.) from JSPS, the Institute for AI and Beyond (to K.O.), and the World Premier International Research Center Initiative (WPI) from MEXT.

Author contributions: All experiments were organized by H.K. T.S. led the team (S.Z., H.O., T.A., M.O. and S.K.P.) for synapse-tool design, validation and behavioral application. H.K. and S.Y. provided guidance. T.H., and K.O. led visual-cortical experiments. S.T., M.K. and M.M. contributed to motor-cortical experiments. The manuscript and figures were prepared jointly by all authors.

Competing Interest: The authors declare no competing interest in this study.

Data and code availability: All data are available in the main text or the Supplementary Materials. DNA plasmids of SYNCit-C (SynC-fusion) and SYNCit-dGAP (SynC-dGAP-fusion) are deposited at Addgene (ID 248572 and 248573). The code used for the model simulations is available at https://github.com/tkssawada/SynC.

Supplementary Materials

Materials and Methods

Supplementary Text

Figs. S1 to S9

Tables S1 to S2

References 51 to 55

Movies S1 to S16

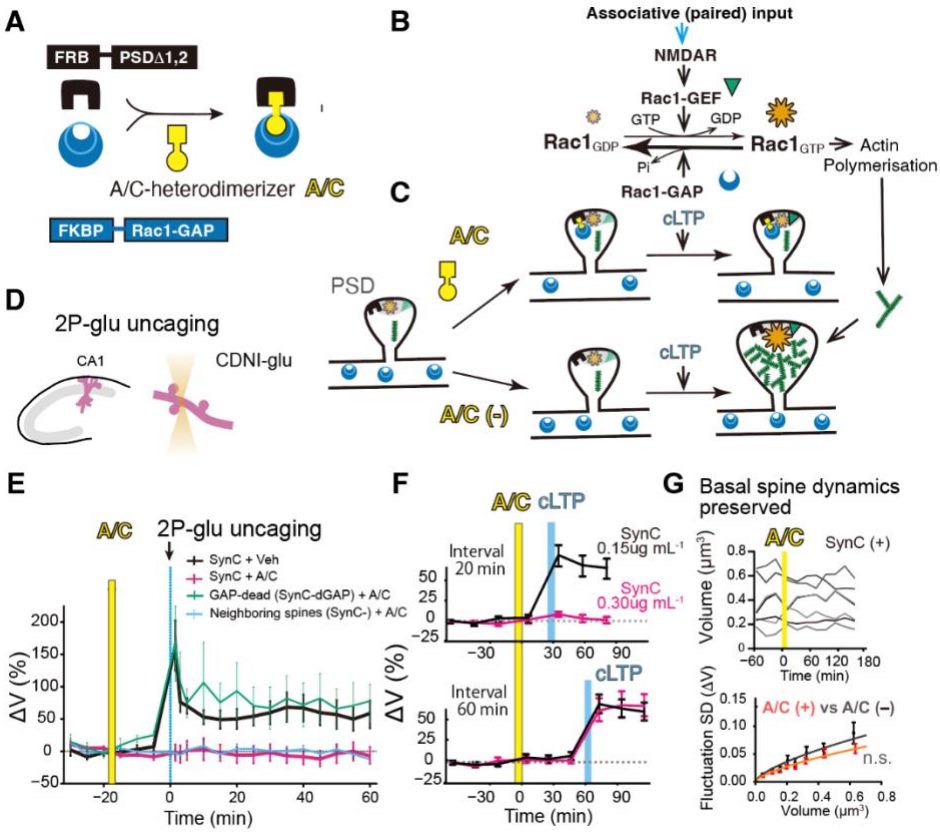

Fig. 1. A/C-triggered SynC blocks rapid spine enlargement.

(A) The A/C heterodimerizer induces FRB–FKBP dimerization.

(B) Rac1 cycling: a GEF activates Rac1 by GTP loading, whereas a GAP inactivates Rac1 by catalyzing GTP hydrolysis.

(C) SynC design. FRB is anchored at the postsynaptic density (PSD) via PSDΔ1,2, and FKBP–Rac1-GAP is cytosolic. Without A/C, endogenous Rac1 signaling permits enlargement; A/C recruits Rac1-GAP to the PSD, suppressing Rac1-GTP and preventing enlargement.

(D) Two-photon glutamate uncaging of a spine in organotypic rat hippocampal slice cultures (CA1) transduced with AAV::SynC (fig. S2A).

(E) Uncaging-evoked spine enlargement is blocked by A/C in SynC-expressing spines but not in the GAP-dead control (SynC-dGAP); neighboring spines are unaffected. n = 10 spines (SynC + vehicle), 7 spines (SynC + A/C), 12 neighboring spines (+A/C), and 7 spines (SynC-dGAP + A/C). Exact statistics (test statistics, degrees of freedom, and P values) are provided in Fig. S2B.

(F) The blockade recovered by ~60 min after A/C (see fig. S3). SynC was expressed by transfection with SynC plasmid at 0.15 or 0.30 μg mL^{-1} (DNA concentration).

(G) Basal (non-associative) dynamics spared. Basal spine dynamics are preserved upon SynC activation. Top, representative traces of spine volume fluctuations (ΔV) in SynC-expressing spines aligned to A/C application. Bottom, fluctuation SD (ΔV) as a function of spine volume comparing A/C (+) and A/C (−) conditions (n.s.; see Fig. S3E for full quantification and additional metrics).

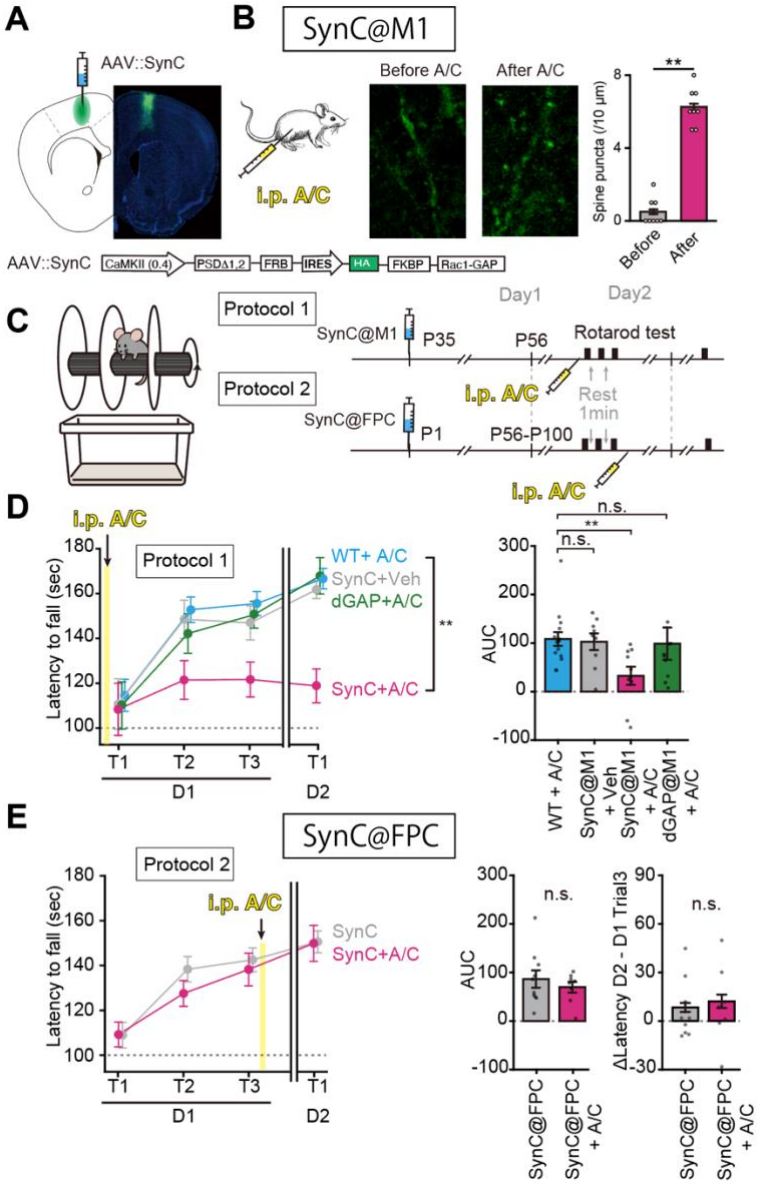

Fig. 2. Behavioral consequences of SynC expression in M1 (A-D) and frontoparietal cortex (E).

(A) Bilateral injection of AAV::SynC into M1 and representative coronal section showing expression.

(B) Immunohistochemical detection of the HA tag in M1 dendrites before and 30 min after i.p. A/C. Right, HA-positive spine puncta per 10 µm (8 dendritic segments from 4 mice [before] and 8 dendritic segments from 2 mice [after]). Mann–Whitney, U = 6, P = 0.0015. Scale bar, 1 µm.

(C) Rotarod task and experimental protocols. Protocol 1, A/C before training (acquisition test). Protocol 2, A/C after Day 1 training (post-training/performance test).

(D) Protocol 1 in SynC@M1: learning curves showing latency to fall. Group sizes: n =

15 WT + A/C, 8 SynC@M1 + vehicle, 10 SynC@M1 + A/C, and 11 SynC-dGAP@M1 + A/C. Kruskal–Wallis, H = 10.54, P = 0.015; Steel's post hoc vs WT + A/C: SynC@M1 + vehicle, P = 0.57; SynC@M1 + A/C, P = 0.0082; SynC-dGAP@M1 + A/C, P = 0.298.

(E) Protocol 2 in SynC@FPC: overnight improvement was unaffected when A/C was administered after the initial training session (n = 10 A/C[–], 8 A/C[+]). Error bars, mean ± s.e.m. Mann–Whitney (A/C after Day 1 training): AUC, U = 44, P = 0.76; Δlatency, U = 32.5, P = 0.53.

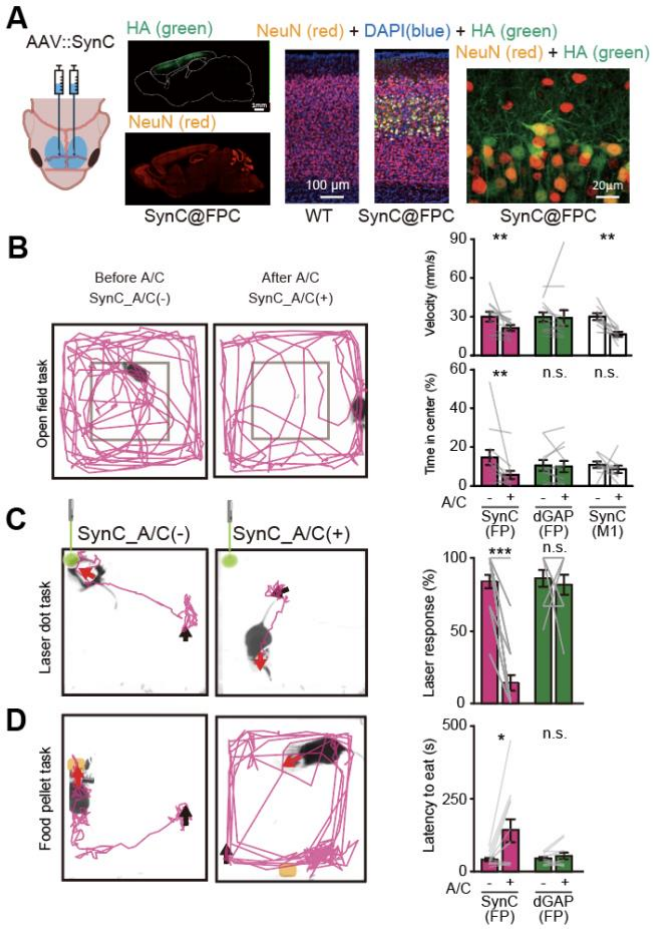

Fig. 3. SynC activation in frontoparietal cortex disrupts goal-directed behavior.

(A) Neonatal bilateral cortical injection of AAV::SynC and representative sagittal sections at 10 weeks. SynC was detected by anti-HA (green) and neurons by anti-NeuN (red); DAPI (blue). Scale bars, 1 mm (sagittal), 100 µm (magnified), and 20 µm (high magnification).

(B) Open-field trajectories before and after i.p. A/C. Quantification of running velocity and time spent in the center. Group sizes: n = 12 SynC@FPC, 12 SynC-dGAP@FPC, and 10 SynC@M1. Bonferroni-corrected Wilcoxon signed-rank tests (velocity): SynC@FPC, P = 0.00684, W = 6; SynC-dGAP@FPC, P = 0.151, W = 20; SynC@M1, P = 0.00195, W = 0. (Time in center): SynC@FPC, P = 0.00684, W = 6; SynC-dGAP@FPC, P = 0.970, W = 38; SynC@M1, P = 0.0840, W = 10.

(C) Laser-dot chasing task. Representative trajectories and laser response rate (n = 26 SynC@FPC and 11 SynC-dGAP@FPC). Bonferroni-corrected Wilcoxon signed-rank tests: SynC@FPC, P = 8.93 × 10−6, W = 0; SynC-dGAP@FPC, P = 0.680, W = 6.

(D) Food-pellet initiation task. Representative trajectories and latency to eat (n = 12 SynC@FPC and 11 SynC-dGAP@FPC). Bars show mean ± s.e.m. For (B–D), analyses were performed in animals meeting predefined State-C criteria. Bonferroni-corrected Wilcoxon signed-rank tests: SynC@FPC, P = 0.0210, W = 10; SynC-dGAP@FPC, P = 0.413, W = 23.

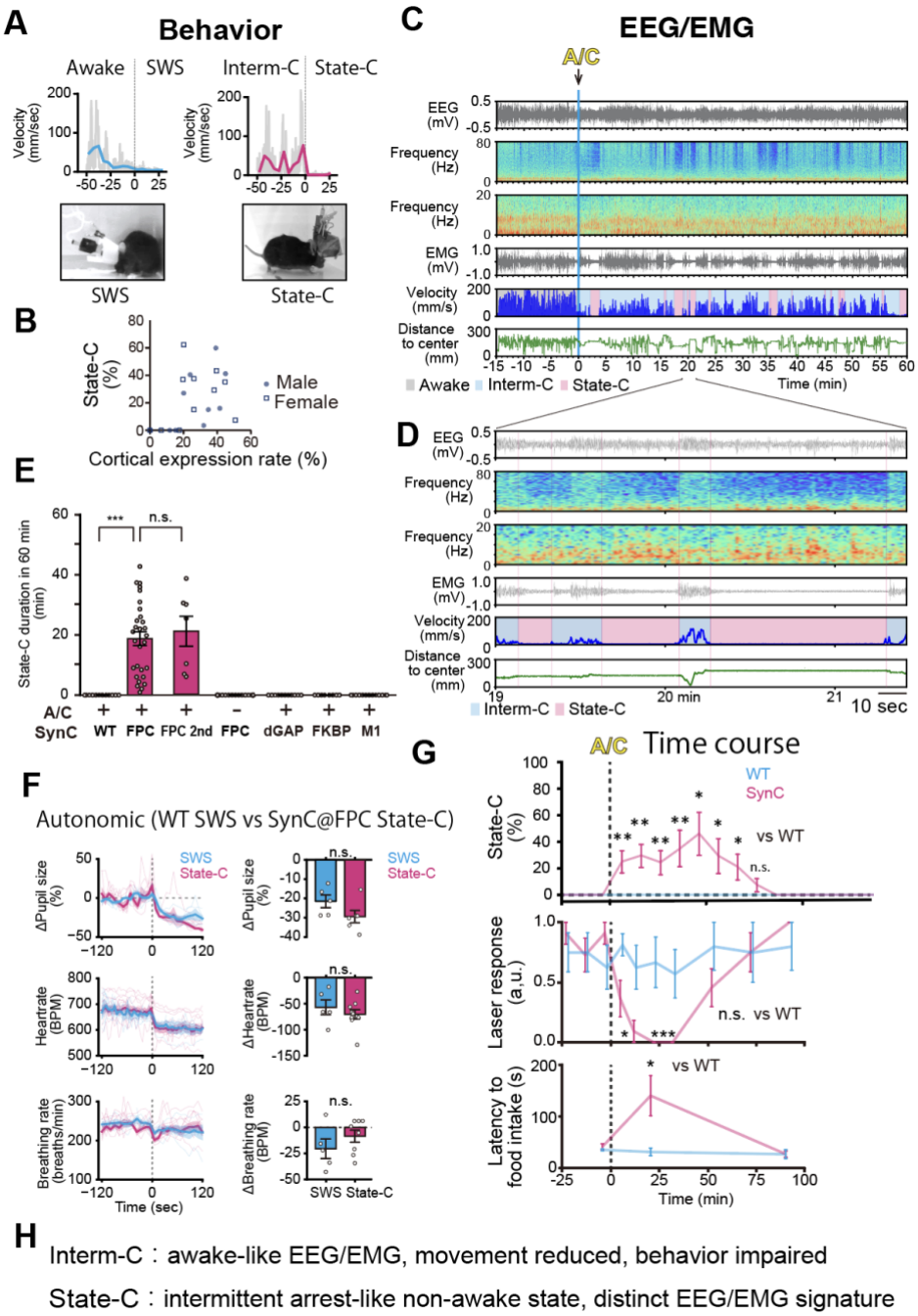

Fig. 4. Definition and physiological signature of State-C.

(A) Example transitions from Awake into slow-wave sleep (SWS) in wild-type (WT) mice and from Interm-C into State-C in SynC@FPC mice, showing locomotor velocity and posture.

(B) Cortical SynC expression versus cumulative State-C duration within 1 h after A/C (n = 21 mice); mice with <20% expression show no State-C (n = 5).

(C) Representative EEG/EMG recordings, power spectra, and state classification before

and after i.p. A/C.

(D) Interm-C→State-C transition showing abrupt suppression of γ-band power and spindle-like events without a sustained increase in δ power.

(E) Cumulative time spent in State-C during the first hour after A/C across groups. dGAP stands for SynC-dGAP and FKBP for FKBP-GAP.

***, WT +A/C vs SynC@FPC +A/C; n.s., SynC@FPC +A/C vs SynC@FPC +A/C 2nd.

(F) Autonomic changes during transitions into State-C (pupil and heart rate, n = 12 each; respiration, n = 20) compared with WT SWS transitions (n = 10). Mann–Whitney tests (State-C vs WT SWS transitions): pupil, U = 70, P = 0.70; heart rate, U = 68, P = 0.81; respiration, U = 74, P = 0.85.

(G) Time course after A/C showing State-C occupancy, laser-dot responses, and latency to eat (sample sizes as indicated). State-C occupancy (Bonferroni-corrected Mann–Whitney vs WT): P = 0.0028, U = 9 (5–35 min); P = 0.0086, U = 13.5 (45–55 min); P = 0.024, U = 18 (65 min). Laser-dot responses: Friedman, $\chi^2 = 27.8$, P = 4.05×10^{-6}; post hoc Wilcoxon vs baseline: 0–10 min, P = 0.0047, W = 0; 10–30 min, P = 9.8×10^{-4}, W = 0. Feeding initiation: Friedman, $\chi^2 = 11.48$, P = 3.2×10^{-3}; post hoc Wilcoxon vs baseline at 20 min, P = 0.021, W = 10. Mean ± s.e.m.

(H) Operational definitions of Interm-C and State-C used throughout the figure.

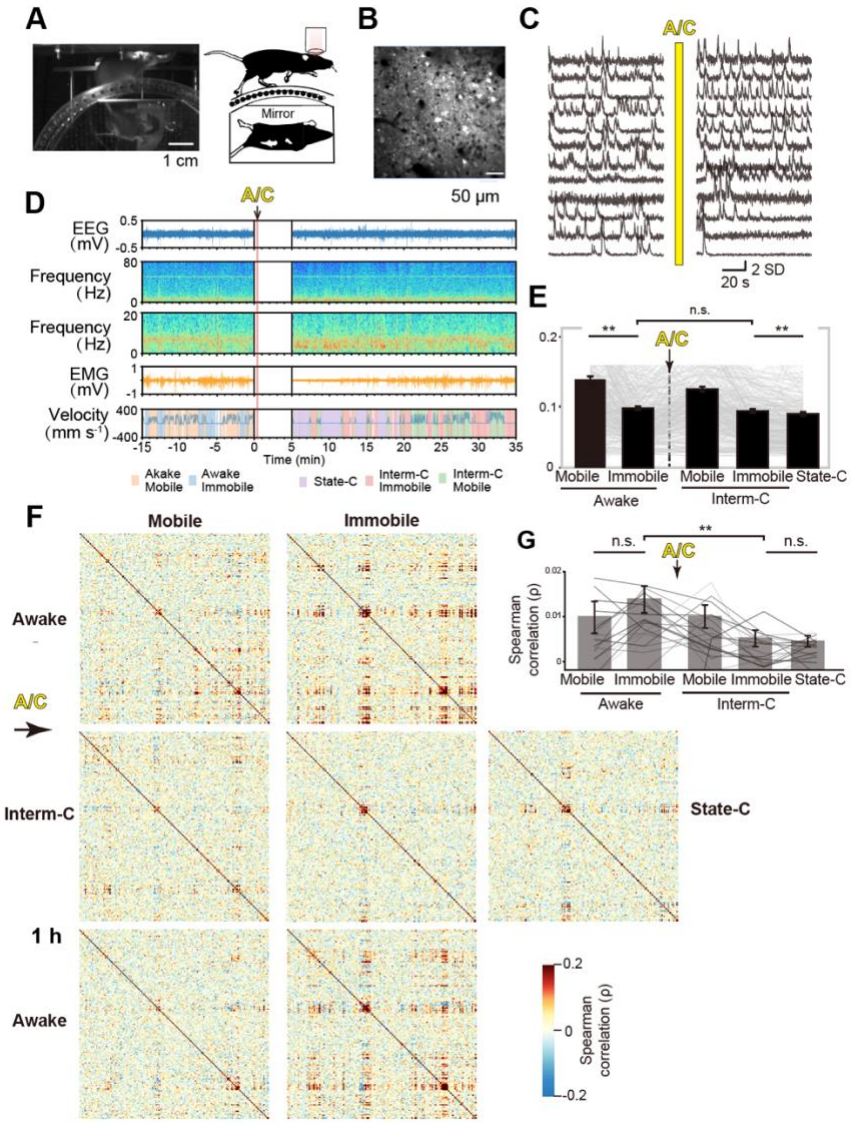

Fig. 5. FPC SynC activation reduces M1 ensemble correlations during Interm-C and State-C.

(A) Treadmill setup for two-photon calcium imaging in head-fixed mice.

(B) Representative field of view of GCaMP7f-expressing neurons in M1. Imaging was performed during the animals' active (dark) phase. Scale bar, 50 µm.

(C) Representative GCaMP7f fluorescence traces from individual M1 neurons.

(D) Simultaneously recorded M1 EEG, EEG power spectra (0–80 Hz and 0–20 Hz), EMG, and locomotor velocity. Color-coded bars indicate behavioral state classification (Awake: mobile/immobile; Interm-C: mobile/immobile; State-C).

(E) Inferred firing-rate changes across behavioral states from calcium imaging (493 cells from 5 SynC@FPC mice). Gray lines indicate within-cell changes across states; bars show mean ± s.e.m.

(F) Pairwise Spearman correlation matrices for 177 neurons from one representative mouse across mobile and immobile states before and after A/C. Matrices are shown after hierarchical clustering to visualize ensemble structure.
(G) Mean pairwise Spearman correlation coefficients summarized across neuronal assemblies (21 assemblies from 5 mice). Statistical tests and exact P values are provided in Methods. Bars and lines show mean ± s.e.m.

677 # Materials and Methods

678

679 ## Animals

680 Dissociated cortical neuron cultures were prepared from embryonic day 17 (E17) ICR
681 mouse embryos (Japan SLC). Sprague–Dawley rats (Sankyo Lab Service) were used to
682 prepare organotypic slice cultures. Neurons from both sexes were mixed in these
683 experiments.

684 For SynC@FPC experiments, 151 male and 162 female C57BL/6J mice (Sankyo
685 Lab Service) received viral injections at postnatal day 1 (P1). Because sex
686 determination at P1 is impractical, both sexes were included, and data from males and
687 females were pooled since no significant sex differences were observed (e.g., Fig. 4B).
688 Thy1-GCaMP6s transgenic mice (C57BL/6N background, Japan SLC) were used for
689 Ca^{2+} imaging experiments in visual cortex (V1). Male C57BL/6J mice aged 4–5 weeks
690 were used for rotarod experiments. In the V1 and M1 experiments, we included only
691 males to ensure consistency with existing normative datasets and to minimize animal
692 numbers, as these paradigms were not specifically designed or statistically powered to
693 detect sex differences.

694 Animals were housed under controlled temperature and humidity conditions and
695 typically maintained on a 12-h light/dark cycle. At the time of experiments, animals
696 were 8–17 weeks old. Food and water were provided ad libitum, except for experiments
697 shown in Fig. 4, Fig. 5, and fig. S9, where the light/dark cycle was reversed to assess
698 behavioral performance during the animals' active (night) period. No formal
699 randomization was performed; however, P1 viral injections were carried out across
700 multiple litters and days without selection for sex, litter, or injection order, effectively
701 randomizing animals across experimental groups. All experimental procedures were
702 approved by the Animal Experimental Committee of the Faculty of Medicine, The
703 University of Tokyo.

704 Plasmid constructions and adeno-associated virus (AAV) preparation

705 For dissociated neuronal cultures, the following constructs were generated by PCR and
706 In-Fusion cloning (Takara Bio):
707 pAAV-CaMKII(0.4)-Cre-W; pAAV-hSyn-DIO-mScarlet-W; pAAV-hSyn-DIO-
708 PSDΔ1,2-FRB×3-W; pAAV-hSyn-DIO-FKBP-mVenus-α1-chimerinGAP-W; pAAV-
709 hSyn-DIO-FKBP-mVenus-α1-chimerinGAP-dead(R179G)-W; and pAAV-hSyn-DIO-
710 PSDΔ1,2-FRB-IRES-FKBP-mVenus-α1-chimerinGAP-W.
711 Human FKBP and FRB, and mouse α1-chimerin (Rac1-GAP) cDNAs were cloned from
712 cDNA templates. The GAP-dead mutant was generated by introducing an R179G

713 substitution into α1-chimerin using the following primers (mutated bases underlined):
714 5′-gagagttacggcgtaccagctgctcctg-3′ and 5′-gtacgccgtaactctctggacagg-3′. PSDΔ1,2 was
715 created by deleting amino acids 65–312 from PSD-95. FRB contained the T2098L
716 mutation, as in SynK (*16*), to reduce binding to endogenous FRB and mTOR.
717 For in vivo experiments, the following constructs were packaged into AAV
718 vectors. GAP denotes the RhoGAP domain (amino acids 143–322) of α1-chimerin:
719 pAAV-CaMKII(0.4)-PSDΔ1,2-FRB-IRES-FKBP-HA-GAP-W; pAAV-CaMKII(0.4)-
720 PSDΔ1,2-FRB-IRES-FKBP-HA-GAP-dead(R179G)-W; pAAV-CaMKII(0.3)-
721 PSDΔ1,2-mVenus-FRB×3-W; and pAAV-CaMKII(0.3)-FKBP-mVenus-GAP-W. The
722 AAV-Syn-jGCaMP7f construct was used for calcium imaging.
723 AAVs were produced and titrated as described previously (*16*). Briefly, plasmids
724 encoding the AAV vector, pHelper (Stratagene), and pUCmini-iCAP-PHP.eB (Addgene
725 #103005) were transfected into HEK293 (AAV293) cells (Stratagene). After three days,
726 cells were harvested and AAV particles were purified twice by iodixanol gradient
727 centrifugation. Viral genome titres were determined by quantitative PCR. SynC-fusion
728 and SynC-dGAP plasmids have been deposited at Addgene (IDs 248572 and 248573).
729

730 **Dissociated culture of neocortex**

731 Cortical neurons were dissociated from embryonic day 17 (E17) ICR mouse embryos
732 and plated at 4.5×10^4 cells cm^{-2} on poly-L-lysine-coated glass-bottom dishes (MatTek,
733 #1.5). Cultures were maintained at 37 °C in 5% CO_2 in Neurobasal medium (Gibco)
734 supplemented with B27 and L-glutamate. At 16 days in vitro (DIV16), cells were
735 transfected with CAG-mScarlet, CaMKII(0.3)-PSDΔ1,2-FRB×3 and CaMKII(0.3)-
736 mVenus-FKBP-GAP at a plasmid ratio of 5:15:1 using Lipofectamine 2000
737 (Invitrogen). After 3–5 days, dual-color time-lapse images (mVenus and mScarlet) were
738 acquired every 20 min using a confocal microscope (A1R, Nikon). Translocation was
739 induced by adding the A/C heterodimerizer (Takara Bio; 0.5 mM stock in ethanol) at a
740 final concentration of 4 μM, followed by three washes after 10 min. Mean spine density
741 did not differ between WT and GAP-transfected neurons (fig. S3E).
742 For analysis of intrinsic spine fluctuations (fig. S3E), the mean change in spine
743 volume (μ) and standard deviation (σ) were computed per 20-min bin during −50 to −10
744 min before and 10 to 130 min after A/C administration (*16*).
745 To induce chemical LTP, neurons were pre-treated with 50 μM D-APV for 12 h
746 before stimulation, then the medium was replaced with a solution containing (in mM):
747 140 NaCl, 5 KCl, 10 D-glucose, 2 $CaCl_2$, 10 HEPES-Na, 200 μM glycine, and 20 μM
748 bicuculline. After 3–10 min, cultures were returned to the original medium.

749 To induce chemical LTD (fig. S3D), neurons were treated with 20 μM NMDA for
750 5 min in the continuous presence of 400 nM muscimol, which promoted spine shrinkage
751 (*48*).
752 For histological examination (fig. S1B), cultured cells were washed with
753 phosphate-buffered saline (PBS, pH 7.4) and fixed overnight in 4% paraformaldehyde
754 in PBS, then stored in PBS. Immunohistochemistry was performed as described in the
755 Histology section.
756

757 **Hippocampal slice culture**

758 Transverse hippocampal slices (350 μm thick) were prepared from postnatal day 6–8
759 Sprague–Dawley male rats and placed on 0.4-μm culture inserts (EMD Millipore).
760 Slices were maintained at 35 °C in 5% CO_2 in culture medium containing 50% MEM
761 (Invitrogen), 25% HBSS (Invitrogen), 25% horse serum (Invitrogen), and 6.5 g L^{-1}
762 glucose.
763 AAV mixtures were injected into area CA1 on the day of or the day after slice
764 preparation under an upright microscope to confine viral spread within CA1. The
765 injected AAVs were as follows: pAAV-CaMKII(0.4)-Cre (5.0×10^9 gc mL^{-1}); pAAV-
766 hSyn-DIO-PSDΔ1,2-FRB×3 (3.0×10^{13} gc mL^{-1}); pAAV-hSyn-DIO- mVenus-FKBP-
767 GAP (2.0×10^{12} gc mL^{-1}); and pAAV-hSyn-DIO- mVenus-FKBP- dGAP (2.0×10^{12} gc
768 mL^{-1}). After 10–12 days in culture, slices were transferred to a recording chamber and
769 superfused with artificial cerebrospinal fluid (ACSF) containing (in mM): 125 NaCl,
770 2.5 KCl, 2 $CaCl_2$, 0 $MgCl_2$, 1.25 NaH_2PO_4, 26 $NaHCO_3$, 20 glucose, and 200 μM
771 Trolox (Sigma-Aldrich), continuously bubbled with 95% O_2/5% CO_2.
772 Spine enlargement was induced in Mg^{2+}-free ACSF as described previously (*5,*
773 *49*). CDNI-glutamate (1 mM; Nard Institute) was bath-applied for 3–5 min, and photo-
774 uncaging was performed near the target spine. Experiments were conducted at 31 °C.
775 Synaptic transmission was recorded from CA1 pyramidal neurons under whole-
776 cell voltage clamp using patch electrodes (5–7 MΩ) filled with internal solution
777 containing (in mM): 120 potassium gluconate, 20 KCl, 10 disodium phosphocreatine, 4
778 ATP (Mg^{2+} salt), 0.3 GTP (Na^+ salt), and 10 HEPES-KOH (pH 7.3). Evoked synaptic
779 currents were averaged from 10 consecutive stimuli and plotted at each time point
780 (Multiclamp 700B amplifier, Molecular Devices).
781 To isolate receptor-specific components, AP5 (50 μM; Abcam) or NBQX (10
782 μM; MedChemExpress) was applied together with bicuculline (20 μM; Fujifilm) at a
783 holding potential of −70 mV for NMDA- or AMPA-receptor-mediated currents,
784 respectively, whereas GABA-mediated currents were isolated at +30 mV in the

presence of AP5 and NBQX. Currents were low-pass filtered at 4 kHz and sampled at 10 kHz. Series resistance was ~20 MΩ (uncompensated), and recordings with resistance >30 MΩ were excluded.

Mouse AAV and A/C injection

All AAV-mediated transductions were performed using the AAV.PHP.eB capsid. For adult mice (4–5 weeks old; Fig. 2), 1 µL of AAV::CaMKII-SynC (1.0×10^{13} gc mL^{-1}) was pressure-injected unilaterally into V1 (AP −3.0 mm, ML +2.0 mm from bregma) and bilaterally into M1 (AP +1.0 mm, ML ±1.0 mm, DV −1.5 mm from the skull surface) at a depth of 200–450 µm using a syringe pump (RWD) at 0.1 µL min^{-1}. Injections were made through borosilicate glass capillaries without filament (B150-86-10; Sutter Instrument) pulled on a P-1000 micropipette puller (Sutter Instrument).

For neonatal mice (postnatal day 1), injection pipettes were fabricated from 10 cm quartz glass capillaries (outer diameter 1.0 mm, inner diameter 0.5 mm; no filament; Q100-50-10, Sutter Instrument) using a P-2000 puller (Sutter Instrument) to yield ~30 µm tip diameters. Each pipette was connected via silicone tubing to a 25 µL Hamilton syringe (1702 RN). Viral injections were performed in 250 pups at postnatal day 1 (P1). Each pup was anesthetized by brief hypothermia on an ice bed and secured in a custom neonatal head holder (Narishige; designed by Mr. Ooishi). The holder arms were positioned vertically at bregma level along the anterior–posterior axis, 0.3 mm lateral to the midline on both hemispheres. The glass micropipette was advanced perpendicularly through the skull to a depth of 350–400 µm, and 4 µL of AAV solution was injected using a syringe pump (Neurostar). After recovery on a heating pad, pups were returned to their home cage. The procedure required less than 20 min per pup.

The A/C heterodimerizer (Takara Bio) was dissolved in N,N-dimethylacetamide (Fujifilm) at 20 mg mL^{-1} and diluted in propylene glycol (Nacalai Tesque) to 2 mg mL^{-1}. Before use, this stock was diluted to 0.4 mg mL^{-1} in diluent (1.2% Polysorbate 80, Fujifilm; 27% PEG-300, Fujifilm) (*50*) and injected intraperitoneally at 2 mg kg^{-1} body weight.

For Ca^{2+} imaging (Fig. 5 and fig. S9), AAV::SynC-fusion (1.2×10^{13} gc mL^{-1}) and AAV::syn-jGCaMP7f (2.0×10^{12} gc mL^{-1}) were co-injected into neonatal pups.

Vital signs

EEG, EMG and heart rate (HR) signals were recorded in an electrically shielded open field using a preamplifier (CerePlex Direct, Blackrock) connected to the main amplifier

820 via a lightweight cable. The preamplifier, connected via a 6- or 8-pin adaptor, was
821 secured to the skull using dental cement.
822 At 8–10 weeks of age, mice were implanted with EEG and EMG electrodes under
823 isoflurane anesthesia. EEG electrodes were placed over the frontal cortex (AP +1.0 mm,
824 ML +1.5 mm from bregma), with the ground electrode attached to the skull over the
825 cerebellum. EMG was recorded from two wire electrodes inserted into the m.
826 trapezoideus. To reduce mechanical noise when the mouse bumped into the wall, the
827 EEG/EMG preamplifier was enclosed in a plastic protective frame.
828 EEG signals were filtered at 0.3–250 Hz using a four-pole Butterworth filter and
829 fast-Fourier-transformed to obtain power spectra (0.5-Hz resolution; absolute power in
830 μV^2 $[0.5\ Hz]^{-1}$). Heart rate (HR) was monitored via two subcutaneous wire electrodes,
831 one placed anterior to the heart and the other in the m. pectoralis major, connected to
832 the EEG preamplifier. Data were displayed online and analysed offline using custom
833 Python scripts.
834 Respiration, body temperature and pupil size were monitored in head-fixed mice
835 on a custom turntable (Thorlabs). Running speed was measured using a rotary encoder
836 (Omron). Respiration was detected with a subcutaneous thermocouple electrode placed
837 beneath the nose, and temperature fluctuations were converted to respiratory traces
838 (PTW-401, Unique Medical). Posture and pupil size were video-recorded and quantified
839 using DeepLabCut with custom Python routines.
840
841 **Behaviors**
842 Behavioral experiments were conducted in mice aged 8–17 weeks. Animals were
843 maintained on a 12-h light / 12-h dark cycle, except for the cohorts used in Fig. 4G and
844 Fig. 5, in which the cycle was inverted so that the animals' dark phase occurred during
845 the local daytime. Only male mice were used for visual cortical and rotarod experiments
846 to minimize variability due to hormonal cycles.
847 ***Visual cortex imaging***
848 For V1 experiments, male mice were anesthetized with isoflurane (5% for induction,
849 1.0–1.5% for maintenance), and a midline scalp incision was made. A custom metal
850 head plate was attached to the skull with dental cement (Super-Bond, Sun Medical). A
851 circular craniotomy (4 mm diameter) was made over the left visual cortex (1 mm
852 anterior and 3 mm lateral to the lambda), and the window was sealed with a glass
853 coverslip. Before imaging, chlorprothixene (1.0 mg kg^{-1}; Sigma-Aldrich) was
854 administered intramuscularly, and isoflurane concentration was reduced to 0.2–0.5%.

855 Wide-field calcium imaging was performed using a macro zoom microscope (MVX10,
856 Evident) equipped with a 2× objective (NA 0.25, MVX Plan Apochromat). GCaMP6s
857 fluorescence was excited with a mercury lamp through a GFP mirror unit (U-
858 MGFPHQ/XL; excitation 488 nm, emission 507 nm; Evident). Fluorescence images (4
859 × 4 mm field of view; 512 × 512 pixels) were acquired at 5 Hz using an sCMOS camera
860 (Zyla 4.2, Andor). Drifting grating stimuli (40° diameter) were presented at three
861 horizontal positions on a 32-inch LCD monitor (20 cm from the right eye) using
862 PsychoPy.
863 For each trial, baseline fluorescence (F) was defined as the mean fluorescence
864 during the 1-s period before stimulus onset. The visual response (ΔF) was defined as the
865 mean fluorescence during the stimulus period, and ΔF/F maps were averaged across
866 trials to generate response maps. Imaging data were analysed using custom MATLAB
867 scripts (MathWorks).
868 ***Motor learning***
869 For motor learning (Fig. 2), male mice were trained on a rotarod (MK-610K,
870 Muromachi). Before training, mice were habituated to the stationary rod until calm for
871 ~2 min. During training, the rod accelerated linearly from 0 to 80 rpm over 300 s. Each
872 mouse underwent three 5-min sessions per day. Motor learning consolidation was tested
873 on the following day with one accelerating trial (0–80 rpm).
874 ***State definitions***
875 **State-C** epochs were defined as post–A/C periods in SynC@FPC mice with sustained
876 behavioral arrest and reduced muscle tone (EMG) that did not meet criteria for NREM
877 or REM sleep.
878 **Interm-C** epochs were defined as post–A/C periods in SynC@FPC mice excluding
879 State-C epochs; quiet immobile epochs within Interm-C were selected by the presence
880 of γ-waves.
881 ***Open-field tasks***
882 Open-field tests were performed either in a large arena (35 × 35 cm) to measure running
883 velocity (Fig. 3) or in a smaller arena (19.4 × 19.4 cm) for close-up videography of laser
884 chasing, food-pellet feeding, and State-C behaviors (Movies S1–S16).
885 For the **laser-dot task**, a green laser pointer (0.5 mW; Sanwa) was projected onto
886 a corner of the small open field for 5 s. A trial was scored as successful (1) if the mouse
887 chased the dot at least once in four presentations, thereby excluding the possibility that
888 the mouse simply failed to attend to the stimulus. WT mice typically chased the laser
889 dot on the floor, whereas SynC@FPC mice neglected it. We eventually used the corner

of the field for projection because laser reflections from the floor often produced multiple spurious dots that occasionally complicated interpretation.

For the food-pellet task, a regular food pellet was dropped into the arena, and the latency from pellet introduction to the first bite while grasping the pellet was measured. Latency measurements excluded time spent in State-C, which was identified from posture and EEG/EMG. SynC@FPC mice often approached and sniffed the pellet but failed to initiate grasping.

In some video recordings, EEG cables were omitted, and State-C was judged solely from behavior.

Treadmill

A custom treadmill system was used to monitor locomotion and posture during two-photon Ca^{2+} imaging of M1 activity (*51*). The treadmill wheel was mounted on translation stages allowing movement along the caudal–rostral and medial–lateral axes, and the head-fixation height was adjustable. A 45° mirror inside the wheel enabled high-speed videography (Basler acA1920-40um) of simultaneous ventral and lateral views.

Wheel rotation was monitored by a rotary encoder (E6B2-CWZ3E, 100 P/R; Omron), and pulses were recorded with CerePlex Direct (Blackrock). The cranial window used a "glass-plug" configuration (51) consisting of two stacked coverslips: a 3-mm-diameter, #1-thickness coverslip placed over a 2-mm-diameter, #3-thickness coverslip (Matsunami Glass) (*52*).

Because behavioral identification was difficult under head fixation, EEG γ-band and EMG signals were used to distinguish State-C from immobile Interm-C. Wheel angular velocity was recorded at 2 kHz and synchronized with imaging via TTL pulses.

In vivo two-photon imaging

For cranial-window surgery for SynC@V1 mice, 8-week-old mice were anesthetized under isoflurane (5% for induction and 1.0–1.5% for maintenance during surgery) and secured as described above. A circular cranial window was made with stainless-steel trephines (ϕ 2.3 mm; Fine Science Tools) under continuous perfusion of oxygenated ACSF, then covered with a coverslip (ϕ 2.3 mm, No. 0, Matsunami Glass). The coverslip and a custom head plate (DMM 3D printed) were affixed with dental cement (RelyX Unicem2 clicker, 3M). In vivo two-photon calcium imaging was conducted using a two-photon microscope (AXR-MP, Nikon, Japan) equipped with a 20× objective lens (CFI75 Apochromat LWD 20XC W, Nikon) and a femtosecond laser (Insight DS+; Spectra-Physics) at 950 nm to excite GCaMP6s. Dendritic spines of

926 GCaMP6s-expressing cells were imaged 60–120 μm below the cortical surface. Series
927 of 500–2000 xy images (8× digital zoom, 512 × 512 pixels) were captured before and
928 after A/C application (*53*).
929 Two-photon excitation imaging of SynC@FPC mice was performed with a
930 tunable Ti:sapphire laser at an excitation wavelength of 950 nm, using a
931 (XLPLN25XWMP2, 25×/1.05 NA, Olympus) objective, and a resonant scanner set on
932 the treadmill (Fig. 5A). Images were acquired at 30 Hz from the forelimb region of M1
933 (AP + 0 mm, ML +0.5 mm from bregma). Laser power at the sample did not exceed 50
934 mW, and sessions per mouse were limited to 90 minutes to avoid photodamage.
935 Regions of interest (ROIs) corresponding to neuronal somata (20–180) were extracted
936 with Suite2p (including non-rigid motion correction, ROI detection/classification, and
937 neuropil subtraction). Photobleaching was corrected per ROI by single-exponential
938 fitting to low-activity segments, ΔF/F was computed, and spike trains were inferred
939 with Suite2p's OASIS deconvolution (τ = 400 ms) to obtain firing rates (Fig. 5E).
940

941 **Histology**

942 Three to ten weeks after behavioral experiments, mice were deeply anesthetized with
943 3% isoflurane and perfused transcardially with PBS (pH 7.4), followed by 4%
944 paraformaldehyde (PFA) in PBS. Brains were post-fixed overnight in 4% PFA at 4 °C
945 and then stored in PBS.
946 For HA-tagged probes, free-floating sagittal sections (50 μm) were cut at 0.5,
947 1.35, 2.35 and 3.55 mm from the midline using a vibratome (VT1200, Leica). Sections
948 were rinsed in PBS, blocked for 1 h at room temperature (RT) in 5% normal goat serum
949 (NGS) in PBST (PBS containing 0.2% Triton X-100), incubated in primary antibody
950 solution (5% normal serum, 0.2% Triton X-100 in PBS) for 24 h at 4 °C, and then in
951 secondary antibody solution under the same conditions for 2 h at RT.
952 ***Primary antibodies:***
953 • Mouse anti-HA (Alexa Fluor 488-conjugated, clone 6E2, #2350S; Cell
954 Signaling Technology), 1:200
955 • Mouse anti-HA (clone 6E2, #2367S; Cell Signaling Technology), 1:200
956 • Rabbit anti-NeuN (EPR12753, ab177487; Abcam), 1:400
957 • Mouse anti-phospho-neurofilament-H (SMI-31, NE1022; Sigma-Aldrich),
958 1:1000
959 • Mouse anti-PSD95 (7E3-1B8, MA1-046; Thermo Fisher), 1:500
960 ***Secondary antibodies:***
961 • Goat anti-rabbit IgG (Alexa Fluor 594, #A-11012; Thermo Fisher), 1:500

- Goat anti-rabbit IgG (Alexa Fluor 405, #A-31556; Thermo Fisher), 1:500
- Goat anti-mouse IgG1 (Alexa Fluor 594, #115-587-185; Jackson ImmunoResearch), 1:500

Nuclei were counterstained with DAPI (4′,6-diamidino-2-phenylindole; ab228549, Abcam) and mounted using Vectashield Antifade Mounting Medium (Vector Laboratories, Burlingame, CA, USA), then cover-slipped.

For mVenus-labelled SynC probes (without HA tag), HA staining was omitted. Sections were rinsed in PBS and directly mounted. Whole-brain serial sections were imaged with an epifluorescence microscope (A1R, Nikon). Z-stack images (4 µm steps; 8 µm total for sagittal sections and 17.7 µm for higher magnification views) were aligned and collapsed using NIS-Elements Advanced Research software (Nikon).

Imaging and histological analyses were performed blinded using Fiji/ImageJ. SynC expression levels were quantified as Z-scores relative to the s.d. of unlabelled regions and plotted on the Swanson flat map (fig. S5). Cortical thickness at M1 was 2.55 ± 0.087 mm (mean ± s.e.m., n = 14) for SynC mice and 2.75 ± 0.097 mm (n = 14) for SynC-dGAP mice (Mann–Whitney $U = 65$, $P = 0.06$).

Statistical treatments

Data are presented as individual observations with mean ± s.e.m. Unless otherwise stated, data were first analysed using non-parametric ANOVA (Kruskal–Wallis), followed by non-parametric multiple comparisons (Steel). When appropriate, Friedman tests or Wilcoxon signed-rank tests (non-parametric *t*-tests versus zero) were applied. Resulting *P* values were corrected for multiple comparisons using the Bonferroni method.

For the analysis of pairwise spike correlations, each state or condition within each session was divided into seven non-overlapping windows of 240 frames randomly sampled from the recording. Within each window, ΔF/F traces were temporally binned by three frames. We then computed Spearman's rank correlation (ρ) across cells, extracted upper-triangle coefficients, Fisher-z transformed them, averaged across the seven windows, and back-transformed to obtain the pairwise ρ distribution per condition (Fig. 5F). In parallel, cells were partitioned into batches of 20 cells, and for each batch and window we computed: (i) the batch-mean correlation (Fig. 5G; Fisher-z mean and back-transformed), (ii) the participation ratio (PR), defined as the square of the total variance (sum of eigenvalues) divided by the sum of squared eigenvalues, indicating the effective dimensionality of neural population activity (fig. S9C), and (iii)

PCA on the matrix after per-cell z-scoring, from which we recorded the number of PCs required to explain 50% of the variance (fig. S9D).

Sample sizes were determined empirically based on previous studies and were comparable to those generally used in the field. No formal randomization was performed; however, because P1 viral injections were conducted across multiple litters and days without selection for sex, litter, or injection order, animals were effectively randomized across experimental groups. Behavioral testing and histological analyses were performed under blinded conditions.

Methods References

48. T. Hayama *et al.*, GABA promotes the competitive selection of dendritic spines by controlling local Ca2+ signaling. *Nat Neurosci* **16**, 1409–1416 (2013).
49. G. C. Ellis-Davies, M. Matsuzaki, M. Paukert, H. Kasai, D. E. Bergles, 4-Carboxymethoxy-5,7-dinitroindolinyl-Glu: an improved caged glutamate for expeditious ultraviolet and two-photon photolysis in brain slices. *J Neurosci* **27**, 6601–6604 (2007).
50. G. J. Goldey *et al.*, Removable cranial windows for long-term imaging in awake mice. *Nat Protoc* **9**, 2515–2538 (2014).
51. R. A. Warren *et al.*, A rapid whisker-based decision underlying skilled locomotion in mice. *eLife* **10**, (2021).
52. M. Kondo *et al.*, Multimodal dataset linking wide-field calcium imaging to behavior changes in operant lever-pull task in mice. *Sci Data* **12**, 1264 (2025).
53. K. M. Hagihara, T. Murakami, T. Yoshida, Y. Tagawa, K. Ohki, Neuronal activity is not required for the initial formation and maturation of visual selectivity. *Nat Neurosci* **18**, 1780–1788 (2015).

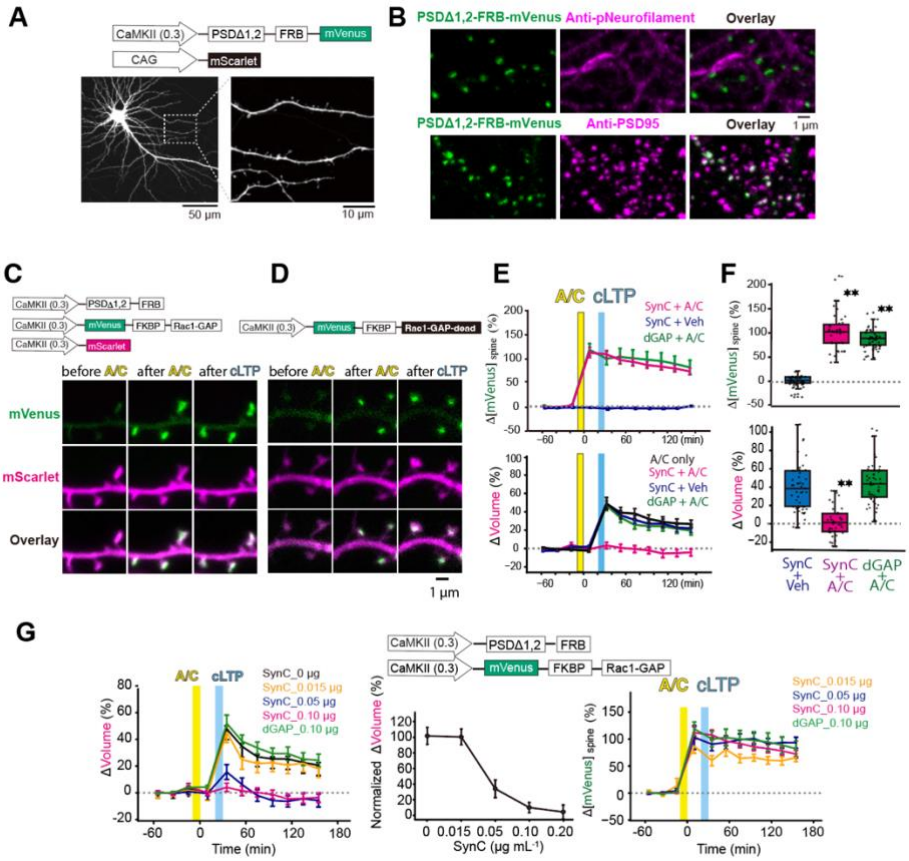

Fig. S1. Validation and specificity of SynC in dissociated neocortical cultures.

(A) Representative dissociated mouse cortical neurons expressing SynC split components (PSDΔ1,2–FRB and FKBP–Rac1-GAP).

(B) Subcellular specificity of PSDΔ1,2–mVenus–FRB (green). PSDΔ1,2–mVenus–FRB colocalizes with the postsynaptic marker PSD95 (bottom) and is excluded from axons labeled by phospho-neurofilament (top). Scale bar, 1 µm.

(C) Top, SynC component constructs under the CaMKII(0.3) promoter. Bottom, representative images of mVenus–FKBP–Rac1-GAP (green) and a volume marker (mScarlet, magenta). A/C application (yellow bar) induces rapid enrichment of mVenus at spines, followed by cLTP induction (blue bar). Scale bar, 1 µm.

(D) GAP-dead control. The GAP-dead mutant translocates to spines after A/C application but does not prevent cLTP-induced spine enlargement.

(E) Time course of spine mVenus enrichment (mVenus fluorescence normalized by the spine volume marker; top) and normalized spine-head volume (bottom). Conditions: SynC + A/C (magenta), SynC + vehicle (black), SynC-dGAP + A/C (green), and A/C only (blue).

1045 **(F)** Summary box plots of spine mVenus enrichment (top) and spine-head volume
1046 change (bottom) at 20 min post-cLTP (same conditions as in E). Boxes show median
1047 and interquartile range; whiskers show min–max. Kruskal–Wallis, $H = 93.18$, $P = 5.85$
1048 $\times 10^{-21}$; Steel's post hoc vs SynC + vehicle, $P < 0.001$ for SynC + A/C; $P < 0.001$ for
1049 SynC-dGAP + A/C. Enlargement: Kruskal–Wallis, $H = 58.88$, $P = 1.63 \times 10^{-13}$; Steel's
1050 post hoc vs SynC + vehicle, $P < 0.001$ for SynC + A/C; $P = 0.599$ for SynC-dGAP +
1051 A/C.
1052 **(G)** Dose dependence of SynC split. Left, time course of spine-head volume change at
1053 varying FKBP–Rac1-GAP concentrations; middle, dose–response summary; right,
1054 spine enrichment of FKBP–mVenus–Rac1-GAP at 20 min after A/C. Sample sizes:
1055 control, 23 dendrites (196 spines); 0.1 μg mL^{-1} GAP, 19 dendrites (151 spines); 0.05 μg
1056 mL^{-1} GAP, 17 dendrites (163 spines); 0.015 μg mL^{-1} GAP, 21 dendrites (164 spines);
1057 0.1 μg mL^{-1} dGAP, 26 dendrites (237 spines). Kruskal–Wallis with Steel's post hoc test
1058 vs control was used; exact statistics are provided in Methods.
1059
1060

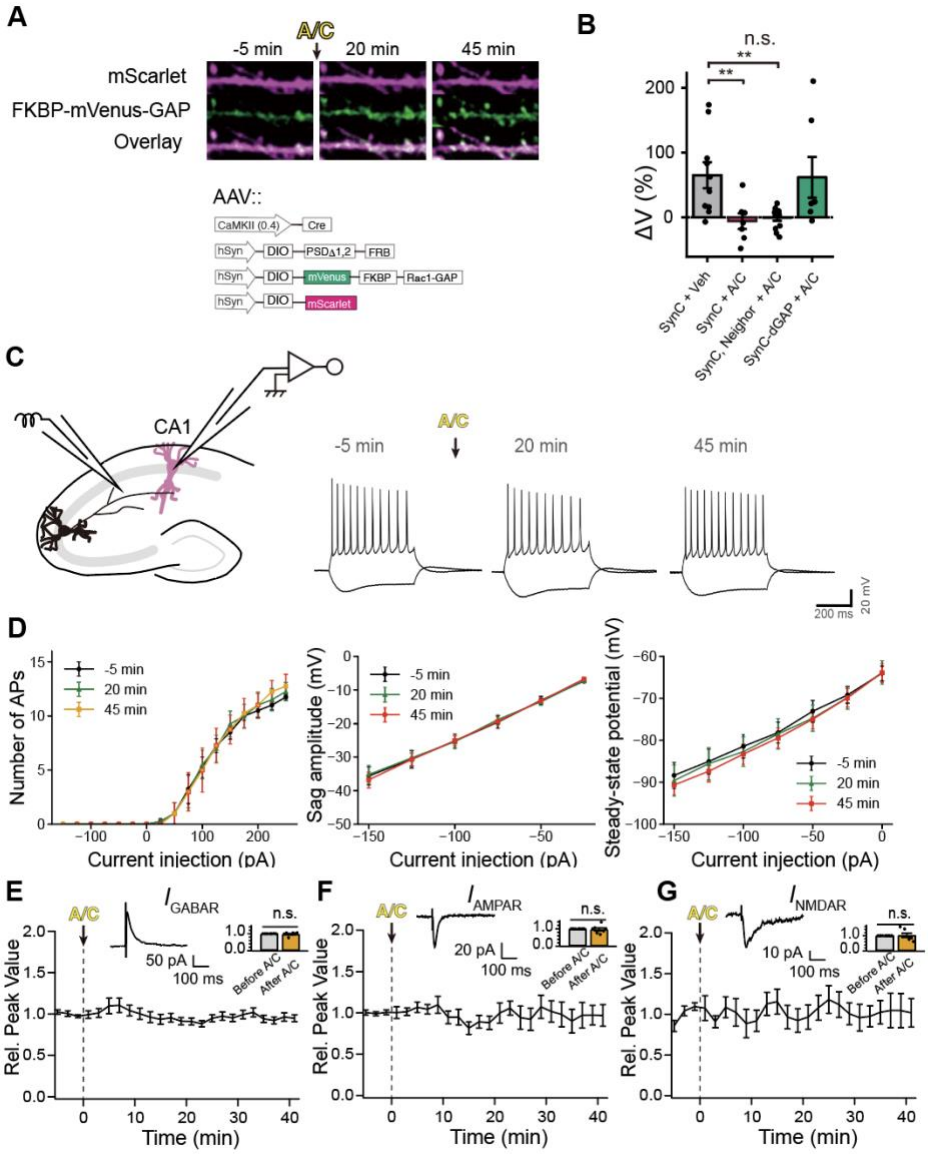

Fig. S2. Baseline neuronal excitability and synaptic currents are preserved after A/C in hippocampal slice cultures.

(A) CA1 pyramidal neurons were transfected with AAVs encoding SynC constructs for 2 weeks (Methods). Filler (mScarlet, left), mVenus-FKBP-GAP (middle) and merged images (right) are shown before and after A/C application.

(B) Exact statistics for Fig. 1E (acute slice spine imaging). Kruskal–Wallis, H = 14.91, P = 1.89 × 10−3; Steel's post hoc vs SynC + vehicle: SynC + A/C, P = 9.26 × 10−3; neighbors (+A/C), P = 8.09 × 10−3; SynC-dGAP + A/C, P = 0.813.

(C) Schematic of the slice-recording configuration for current-evoked action potentials (APs) and electrically evoked synaptic currents. Representative AP trains are shown before and after A/C (times indicated).

1072 **(D)** Intrinsic membrane properties were stable across A/C administration. Summary
1073 plots show the number of APs versus injected current (left), sag amplitude (middle), and
1074 steady-state membrane potential (right) (n = 4 neurons). Two-sided repeated-measures
1075 ANOVA: number of APs, $F(2,6) = 0.096$, $P = 0.91$; sag amplitude, $F(2,6) = 1.22$, $P =$
1076 0.36; steady-state potential, $F(2,6) = 1.34$, $P = 0.33$.
1077 **(E–G)** Synaptic currents recorded in the presence of selective blockers. A/C had no
1078 detectable effect on $GABA_A$ receptor–mediated currents (E; I_{GABAR}), AMPA receptor–
1079 mediated currents (F; I_{AMPAR}), or NMDA receptor–mediated currents (G; INMDAR)
1080 (n = 7 cells each). Wilcoxon signed-rank tests: IGABAR, $W = 12$, $P =$
1081 0.81; I_{AMPAR}, $W = 12$, $P = 0.81$; I_{NMDAR}, $W = 13$, $P = 0.94$. Scale bars, 200 ms and 20
1082 mV (AP traces in C), and as indicated for synaptic-current traces (E–G). Data are mean
1083 ± s.e.m.
1084

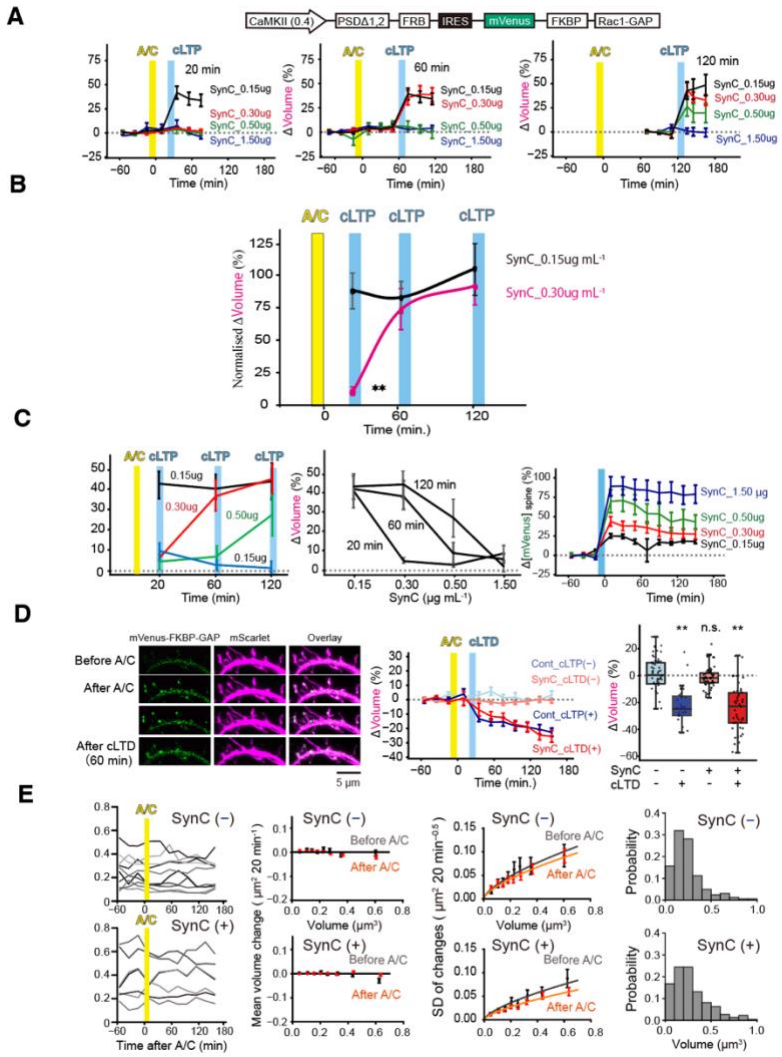

Fig. S3. Functional properties of bicistronic SynC.

(A) Performance of the bicistronic SynC fusion construct (IRES). Spine-head volume change (Δvolume) following cLTP measured at 20, 60, and 120 min after A/C application, together with spine enrichment of mVenus–FKBP–Rac1-GAP.

(B) Repeated cLTP reveals recovery from SynC-mediated blockade. After A/C application, cLTP was delivered repeatedly at the indicated times, showing that the enlargement response recovers over ~60 min (example conditions shown).

(C) Time- and concentration-dependent blockade by bicistronic SynC. Summary of enlargement measured at 20, 60, and 120 min across SynC concentrations (0.15, 0.30, 0.50, or 1.50 μg mL^{-1}) and corresponding spine enrichment of mVenus–FKBP–Rac1-GAP. Sample sizes: n = 15, 16, 17, and 17 dendrites per concentration, respectively.

(D) Specificity for enlargement versus shrinkage. Left, representative images of spine shrinkage induced by chemical LTD (cLTD; 20 μM NMDA). Center, time course of spine-volume changes. Right, SynC activation did not prevent NMDA-induced spine

shrinkage. Kruskal–Wallis with Steel's post hoc test was used (see Methods for exact statistics).

(E) Population quantification of basal spine dynamics (related to Fig. 1G). Baseline spine volume fluctuations were quantified in SynC-expressing spines under A/C (−) and A/C (+) conditions. Metrics include fluctuation SD (ΔV) (and additional measures shown), computed in 20-min windows, with each point representing one spine (n = 84 spines from 7 neurons, 3 mice). After correction for multiple comparisons, no metric showed a significant difference between A/C (−) and A/C (+).

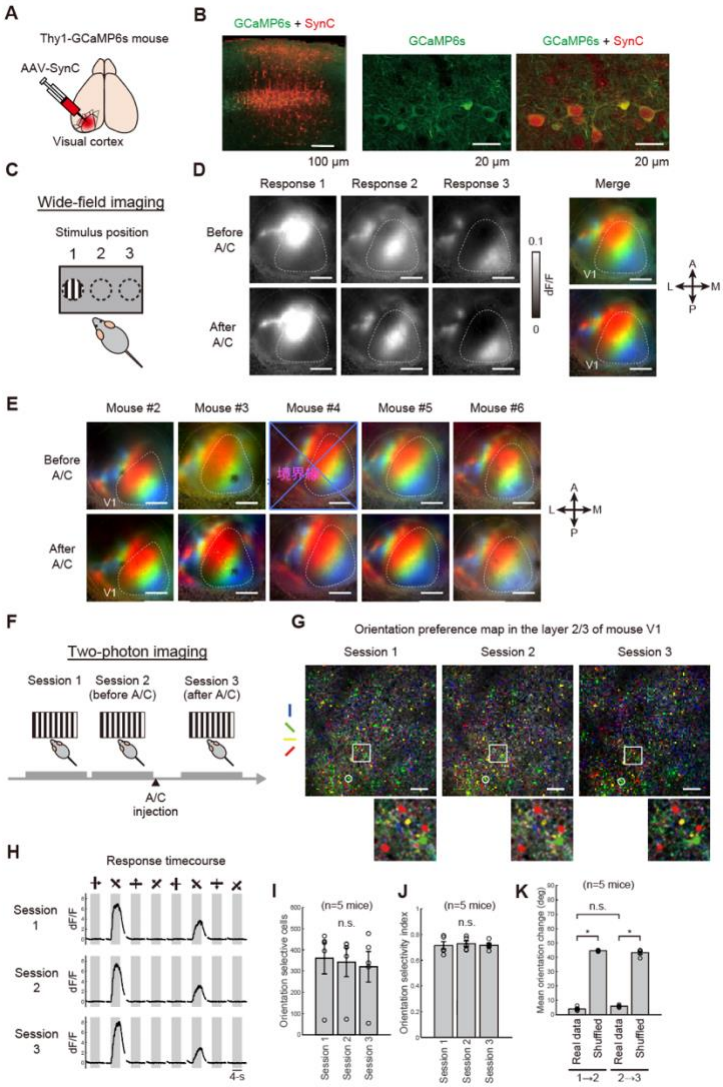

Fig. S4. SynC expression and functional stability in mouse primary visual cortex (V1).

(A) Schematic of AAV::SynC injection into V1 of Thy1-GCaMP6s mice.

(B) Histological verification of GCaMP6s (green) and SynC (red) expression in V1. Scale bars, 100 µm (left) and 20 µm (right).

(C) Wide-field calcium imaging for retinotopic mapping. Drifting grating stimuli (40° diameter) were presented at three horizontal positions.

(D) Representative response maps (ΔF/F) to the three stimuli (left) and merged retinotopic maps (right) before (top) and after (bottom) i.p. A/C. Scale bars, as indicated.

(E) Retinotopic organization across six mice before and after A/C.

(F) Timeline for two-photon calcium imaging in V1 across three sessions to evaluate tuning stability and the effect of A/C.

(G) Orientation-preference maps in layer 2/3 of mouse V1 for sessions 1–3 (top) and magnified views of the indicated regions (bottom). Scale bars, 100 μm.

(H) Trial-averaged calcium traces from a representative neuron (circled in G). Gray shading indicates stimulus presentation (4 s).

(I) Number of orientation-selective neurons across sessions (n = 5 mice; one-way ANOVA, P = 0.96).

(J) Mean orientation selectivity index (OSI) across sessions (n = 5 mice; one-way ANOVA, P = 0.79).

(K) Change in preferred orientation across sessions (n = 5 mice). Preferred orientations were stable relative to shuffled data (paired t test with Bonferroni correction; sessions 1–2, $P = 9.19 \times 10^{-5}$; sessions 2–3, $P = 2.39 \times 10^{-4}$). No difference was detected between control (1–2) and A/C (2–3) intervals (P = 0.569). Error bars show mean ± s.e.m.

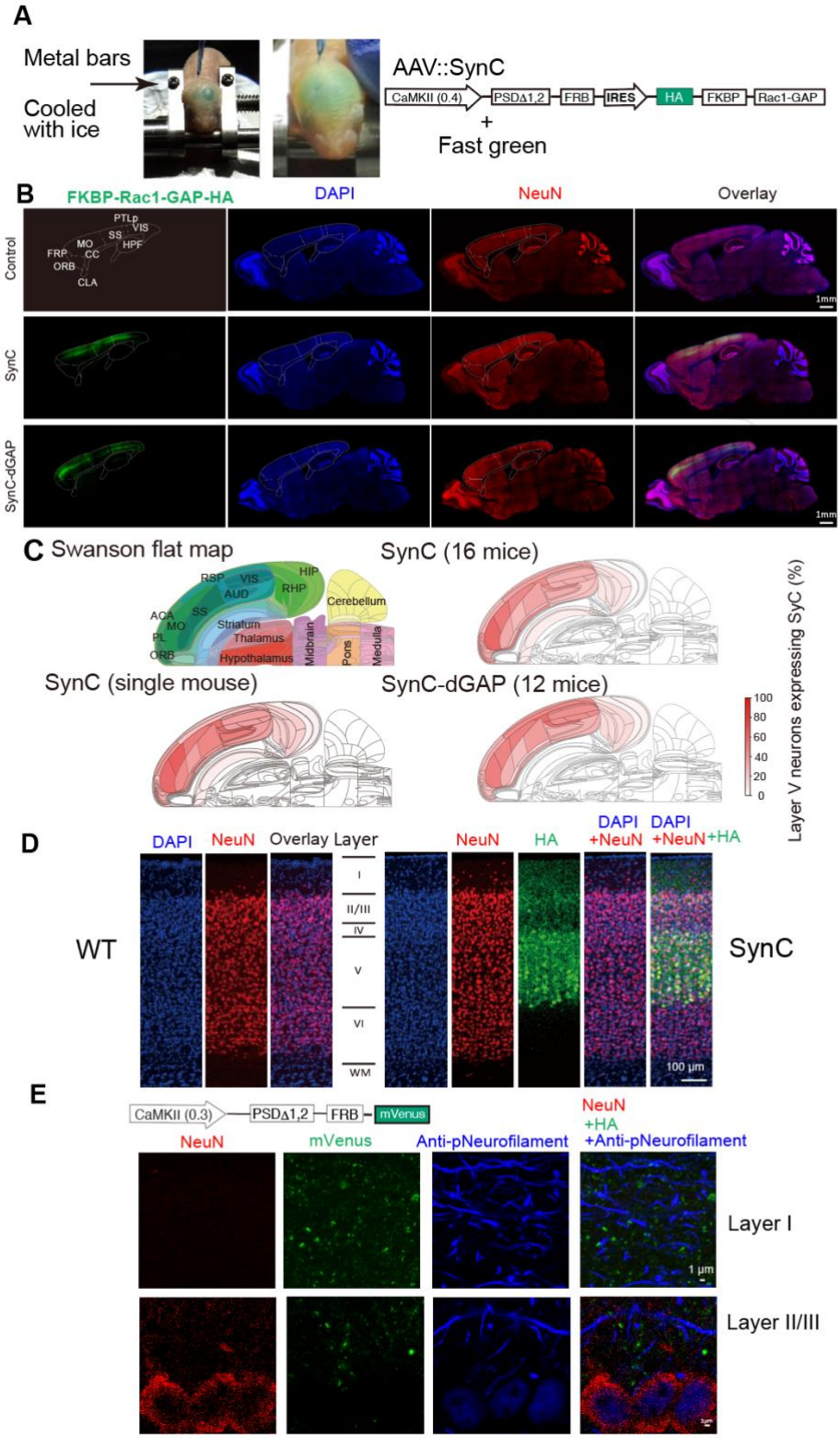

1136 **Fig. S5. Anatomical distribution and cell-type specificity of SynC**
1137 **expression in the neocortex.**

(A) Neonatal mouse pup injection scheme (left) and bicistronic AAV vector design (right). Under the CaMKII(0.4) promoter, the vector drives expression of PSDΔ1,2–FRB and HA-tagged FKBP–Rac1-GAP separated by an IRES. Fast green dye was used to visualize the injection site.

(B) Representative sagittal sections (1.35 mm lateral to midline) from non-injected control, SynC@FPC, and SynC-dGAP@FPC mice. Sections were immunolabeled for HA (green), NeuN (red), and nuclei (DAPI, blue). SynC signal was largely restricted to neocortex, whereas subcortical regions containing long-range cortical axons showed little HA immunoreactivity, consistent with limited axonal transport of the GAP module. Scale bars, 1 mm.

(C) Quantitative mapping of SynC expression across neocortex. Left, Swanson flat map indicating cortical regions. Right, pseudocolor heat maps showing the percentage of HA-positive layer V pyramidal neurons in a representative mouse, the SynC group (n = 16 mice), and the SynC-dGAP group (n = 12 mice).

(D) Enlarged views of M1 lamination in WT and SynC@FPC mice across layers I–VI and white matter (WM). Scale bar, 100 μm.

(E) High-magnification images showing subcellular distribution of PSDΔ1,2–FRB–mVenus (green) relative to NeuN (red) and phospho-neurofilament (blue; axons). In layer I, mVenus-labeled spines are adjacent to axons without overlap with axonal labeling. In layers II/III, mVenus signal is excluded from NeuN-positive somata and is concentrated in dendritic spines, consistent with postsynaptic restriction of the SynC anchor module. Scale bar, 1 μm.

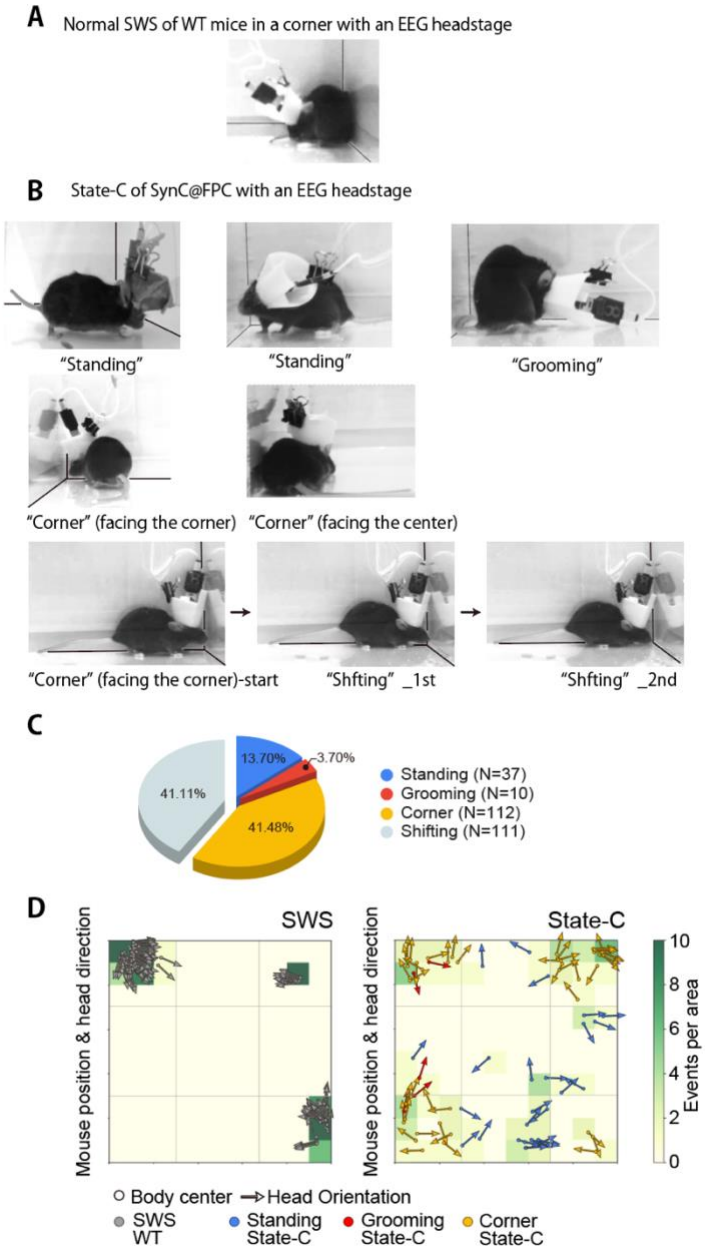

Fig. S6. Behavioral postures and spatial distribution of State-C episodes.
(A) Representative image of a wild-type (WT) mouse during slow-wave sleep (SWS) in the open field.
(B) Representative images of SynC@FPC mice during State-C illustrating four commonly observed postures: standing, grooming, corner, and shifting. In contrast to SWS, State-C episodes occurred during ongoing behavior (e.g., locomotion, grooming, or corner navigation) and were identified by EEG-based state classification. Open-field dimensions, 19.4 × 19.4 cm.
(C) Composition of State-C postures across identified epochs: standing (n = 37),

grooming (n = 10), corner (n = 112), and shifting (n = 111).
(D) Spatial distribution and head orientation during SWS (left; n = 6 mice, 112 epochs) and State-C (right; n = 5 mice, 80 epochs). Dwell time is pseudocolor-coded; arrows indicate body-center position and head orientation. SWS episodes were concentrated near corners, whereas State-C episodes occurred across diverse locations and orientations, consistent with an abrupt behavioral arrest independent of position.

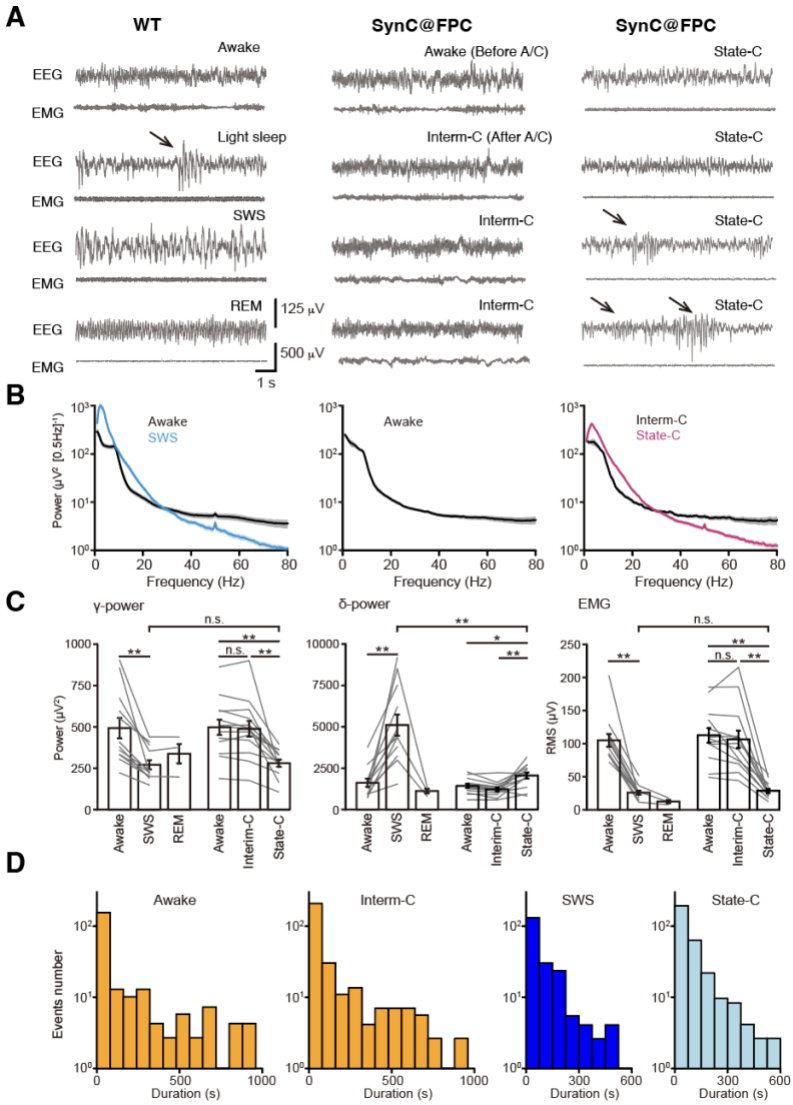

Fig. S7. Comparative EEG and EMG features of awake, sleep, and SynC-induced states.

(A) Representative EEG and EMG traces. WT mice (left) show awake, light sleep, slow-wave sleep (SWS), and REM sleep. SynC@FPC mice (middle) show awake before A/C and Interm-C after A/C. Right, representative State-C episodes after A/C. Arrows indicate spindle-like events observed in both light sleep and State-C. Scale bars, 125 µV (EEG), 500 µV (EMG), and 1 s.

(B) EEG power spectra. Left, SWS (blue) versus awake (black) in WT mice. Middle, awake spectra in SynC@FPC mice before A/C. Right, State-C (magenta) versus Interm-C (black) after A/C. State-C shows reduced γ-band power without the sustained δ-band (0.5–4 Hz) elevation characteristic of SWS.

(C) Quantification of band power and muscle tone across states (n = 12 WT mice; n =

13 SynC@FPC mice). Left, γ power (30–80 Hz) differs across states (Friedman, χ^2 = 19.8, $P = 4.9 \times 10^{-5}$) and is suppressed in State-C relative to awake and Interm-C (post hoc Wilcoxon: awake vs State-C, $P = 2.4 \times 10^{-4}$, $W = 0$; Interm-C vs State-C, $P = 2.4 \times 10^{-4}$, $W = 0$). Middle, δ power (0.5–4 Hz) in State-C is lower than in SWS (Mann–Whitney, $P = 1.7 \times 10^{-4}$, $U = 145$). Right, EMG RMS amplitudes indicate that muscle tone in State-C is reduced relative to awake and remains higher than in REM (Wilcoxon: $P = 2.4 \times 10^{-4}$, $W = 0$).

(D) Episode-duration distributions for awake ($n = 12$), Interm-C ($n = 13$), SWS ($n = 12$), and State-C ($n = 13$). Bars and lines show mean ± s.e.m.

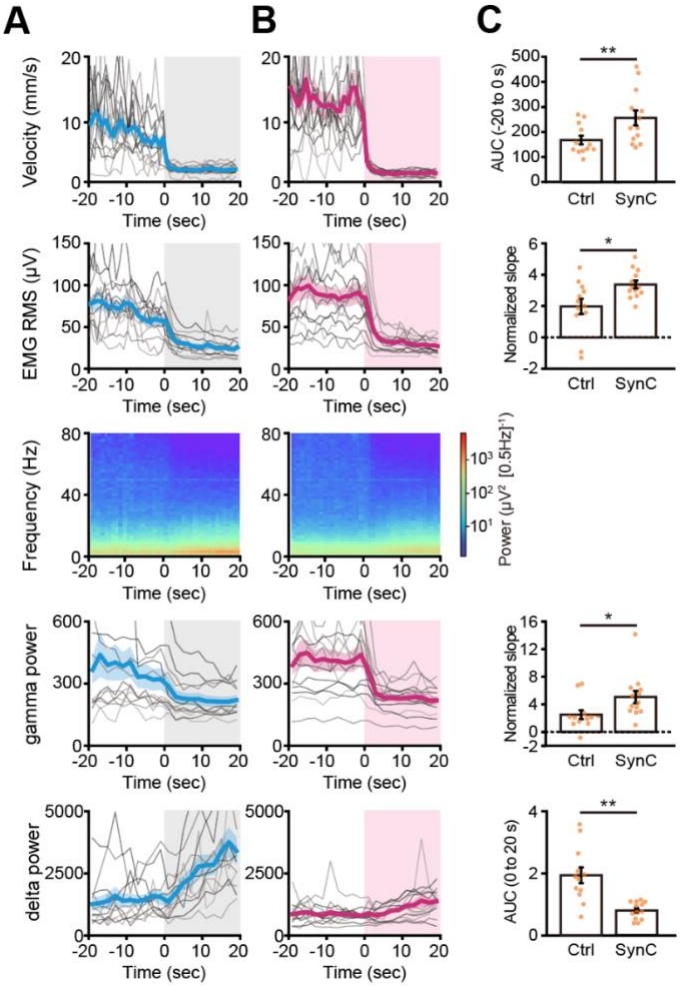

1205 **Fig. S8. Quantitative analysis of abrupt transitions into State-C.**

1206 (A, B) Event-aligned dynamics of behavioral and physiological parameters (top to
1207 bottom: locomotor velocity, EMG RMS, EEG spectrogram, and γ-band [30–80 Hz] and
1208 δ-band [0.5–4 Hz] power). Transitions were aligned to onset (t = 0) of Awake→SWS in
1209 WT mice (A; n = 12) and Interm-C→State-C in SynC@FPC mice (B; n = 13) within 2
1210 h after i.p. A/C. Thin gray traces show per-mouse means (3–16 events per mouse); thick
1211 colored traces show across-mouse means.

1212 **(C)** Quantification of transition dynamics. For each transition, area under the curve
1213 (AUC) was computed for velocity (−20 to 0 s) and δ-band power (0 to 20 s) and
1214 compared between groups using two-sided Mann–Whitney tests (velocity AUC: $P = 4.5$
1215 $\times 10^{-4}$, $U = 32$; δ-band AUC: $P = 0.013$, $U = 143$). Transition abruptness was quantified
1216 as a slope ratio (slope over −3 to +1 s normalized by slope over −10 to +10 s) for EMG
1217 RMS and γ-band power and compared by two-sided Mann–Whitney tests (EMG RMS:
1218 $P = 0.021$, $U = 35$; γ power: $P = 0.013$, $U = 32$). Error bars show mean ± s.e.m.

1219

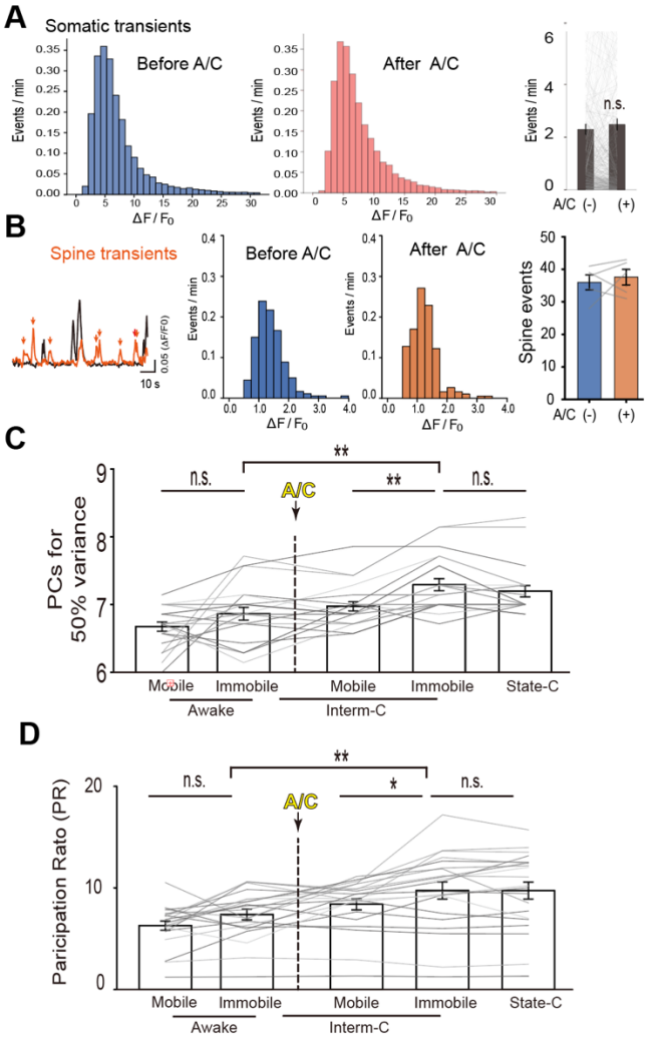

Fig. S9. Stability of calcium signals and dimensionality analyses across A/C and behavioral states.

(A) Distributions of detected somatic GCaMP7f event amplitudes (ΔF/F0) before (blue) and after (red) i.p. A/C, and event rate (events min^−1; right). $n = 493$ cells from 5 mice. Somatic event amplitudes were unchanged after A/C (Wilcoxon signed-rank test: $P = 0.29$, $W = 4.8 \times 10^4$).

(B) Spine calcium signals. Left, representative traces showing spine calcium transients (red) separated from adjacent dendritic shaft signals (black). Right, amplitude distributions and mean spine transient amplitudes were unchanged after A/C (Mann–Whitney test: $P = 0.60$, $U = 9.5$), arguing against a gross reduction in synaptic calcium signals as an explanation for blocked structural plasticity.

(C) Network dimensionality estimated as the number of principal components (PCs) explaining 50% of variance across cells ($n = 21$ neuronal assemblies from 5 mice).

Friedman test with post hoc Wilcoxon signed-rank tests and Bonferroni correction were used (see Methods for exact statistics).

(D) Participation ratio (PR) across behavioral states as an independent dimensionality metric (n = 21 neuronal assemblies from 5 mice). Statistical testing as in **(C)** (see Methods for exact statistics). Bars and lines show mean ± s.e.m.

State (ordered)	Behavior	EEG hallmark	EMG	Autonomic / key discriminator
Awake (reference)	Exploration; goal-directed	Low-amp fast; γ✓; δ low	High	Pupil dilated; HR high-norm; resp ≈;
Interm-C (this study)	**Locomotor-active; goal-directed control ↓**	**Low-amp fast; γ✓; δ low**	**High**	**Pupil/HR ≈; resp ≈; decorrelation↑**
State-C (this study)	**Behavioral arrest with exponential durations, similar to SWS**	**γ↓; small δ↑; isolated spindles sometimes✓; no SWD**	**Low**	**Isolated spindle; Miosis; mild HR↓; resp ≈**
SWS (deep NREM)	Sleep posture; high arousal threshold	δ↑↑; high-amp; spindles ±	Low	Miosis; HR↓; resp slow; high arousal threshold
REM sleep	Twitches / minor moves	θ-dominant; low-amp fast	Very low (atonia-like)	Autonomic variability↑; θ + atonia combo
Freezing (defensive)	Immobility with vigilance	Wake-like; sometimes θ↑	Moderate (rigid-not atonia)	Bradycardia; high vigilance
Absence seizure	Behavioural arrest; brief bouts	7–12 Hz SWD (generalized)	Low–moderate	SWD is defining discriminator
Narcolepsy (incl. cataplexy)	Emotion-triggered collapse; instability	REM-EEG (θ); rapid transitions	Very low during cataplexy	Emotion trigger + REM-EEG + atonia
General anesthesia (propofol)	Unresponsive	δ↑ with frontal α–coherence	Very low	Autonomic suppression; not upright
Catalepsy (neuroleptic-induced)	Waxy flexibility/ Immobility with	Often δ↑; altered coupling reported	Rigid/Increased tone	Drug-induced; no REM-like EEG

Table S1. Differential features distinguishing Interm-C and State-C from canonical sleep, seizure, anesthesia, and arrest-like states.

Entries labeled "this study" were directly observed/defined here. Other entries summarize representative mouse literature (*24-26*). **Notes:** γ, 30–80 Hz; δ, 0.5–4 Hz; θ, 4–8 Hz; SWD, spike-and-wave discharges. See Methods for frequency band definitions and statistics. Upper section summarizes states observed in this study (including Interm-C/State-C and baselines); lower section lists canonical comparator states used for differential classification.

Measure	Awake (reference)	Interm-C	SWS	State-C
Goal-directed behavior	–	↓↓	×	×
Locomotion (gross motor output)	–	↓	×	×
EMG (arousal)	–	≈	↓	↓
EEG γ-power (30–80 Hz)	–	≈	↓	↓
EEG δ-power (0.5–4 Hz)	–	≈	↑↑	↑
Ca^{2+}/spiking rate (gross)	–	≈	↓	↓
Pairwise spike correlation (immobile epoch)	–	↓	↑*	↓
Dimensionality (D_{50})	–	↑	↓*	↑
Dimensionality (PR)	–	↑	↓*	↑

Table S2 State-dependent behavioral and neural signatures (normalized to Awake).

Symbols denote changes relative to Awake (reference): ≈ no detectable change; ↑/↓ increase/decrease; ↑↑/↓↓ marked change; × not observed/not applicable; * based on prior reports (SWS typically shows increased correlations and reduced dimensionality).

Summary (for rapid reading):

Interm-C: γ ≈; mean activity ≈; pairwise correlation ↓; dimensionality ↑.

State-C: mean activity ↓ (SWS-like); γ ↓; δ slight ↑; pairwise correlation ↓; dimensionality ↑.

Definitions: D50, number of principal components explaining 50% of variance; PR, participation ratio.

Data sources: behavioral tasks (Figs. 3–5), EEG/EMG (Fig. 4; fig. S7), Ca^{2+}/spiking and correlations (Fig. 5), dimensionality (fig. S9). *, as reported previously (SWS shows increased correlations and reduced dimensionality) (*28*).

Movie S1. Laser-dot task (WT mouse)

A wild-type (z233) mouse wearing an EEG headset chased a laser dot projected onto the corner of a small open field (19.4 × 19.4 cm) within 10 s. The laser was directed toward the corner to avoid reflections, although mice normally chase the laser dot even on a flat surface. The movie is shown at 2× real time.

Movie S2. Laser-dot task (SynC@FPC mouse before i.p. A/C)

A SynC@FPC mouse (z244-5, 1117 s before A/C) expressing SynC broadly in the frontoparietal cortex chased the laser dot within 10 s, similarly to the WT mouse. The movie is shown at 2× real time.

Movie S3. Laser-dot task (SynC@FPC mouse after i.p. A/C)

The same SynC@FPC mouse (z244-5, 2298 s after A/C) as in Movie 2. The mouse failed to chase the laser dot within 10 s. The movie is shown at 2× real time.

Movie S4. Laser-dot task (SynC@FPC mouse 1 h after i.p. A/C)

The same SynC@FPC mouse (z244-5, 3483 s after A/C) as in Movie 2 and 3. The mouse again chased the laser dot within 10 s, indicating recovery of normal behavior. The movie is shown at 2× real time.

Movie S5. Food-pellet task (WT mouse after i.p. A/C)

A WT mouse (z239, 785 s after A/C) grasped and ate a food pellet placed in the arena within 30 s. The movie is shown at 2× real time.

Movie S6. Food-pellet task (SynC@FPC mouse after i.p. A/C)

A SynC@FPC mouse (z227-6, 1203 s after A/C) repeatedly passed over the food pellet without eating, eventually beginning to consume it only after 5 min. The mouse spent an unusually long period grooming near the pellet and showed no response to the laser dot before finally grasping and eating the pellet. The movie is shown at 2× real time.

Movie S7. Food-pellet task (SynC@FPC mouse 1 h after i.p. A/C)

The same mouse (z227-6, 5204 s after A/C) as in Movie 6. The mouse rapidly approached, grasped, and ate the food pellet within 10 s. The movie is shown at 2× real time.

Movie S8. “Standing” posture example 1 during State-C (SynC@FPC mouse)

A SynC@FPC mouse (z156-3, 444 s after A/C) exhibited a “standing” posture upon behavioral arrest during running, shown from side and top views in a small (15 × 15 cm) open field. EEG, EMG, and velocity traces are displayed simultaneously. The movie is shown in real time.

Movie S9. “Standing” posture example 2 during State-C (SynC@FPC mouse)

A SynC@FPC mouse (z248-2, 1007 s after A/C) exhibited a “standing” posture upon behavioral arrest during running, shown from side and top views in a small (19.4 × 19.4 cm) open field. EEG, EMG, and velocity traces are displayed simultaneously. The movie is shown in real time.

Movie S10. “Grooming” posture during State-C (SynC@FPC mouse)

A SynC@FPC mouse (z248-1, 1873 s after A/C) exhibited a “grooming” posture upon behavioral arrest during grooming, shown from side and top views in a small open field. EEG, EMG, and velocity traces are displayed simultaneously. The movie is shown in real time.

Movie S11. “Corner” posture during State-C (SynC@FPC mouse)

A SynC@FPC mouse (z248-2, 1241 s after A/C) exhibited a “corner” posture upon behavioral arrest while approaching a corner in the small open field. EEG, EMG, and velocity traces are displayed simultaneously. The movie is shown in real time.

Movie S12. “Shifting” posture during State-C (SynC@FPC mouse)

A SynC@FPC mouse (z244-2) exhibited brief “shifting” movements at 115 s and 225 s following a corner posture, coinciding with short bouts (0.5 s and 2 s) of Interm-C. EEG, EMG, and velocity traces are displayed simultaneously. The movie is shown in real time.

Movie S13. Normal sleep-preparation behavior (WT mouse)

Before sleep onset, a WT mouse (z155-2, 1198 s after A/C) slowly walked toward a corner as EEG γ-power was already decreasing. The mouse then turned to face the center, curling its body and tail. EEG δ-power increased after the mouse adopted a full sleep posture. The movie is shown in real time.

Movie S14. Transition from Interm-C to State-C (SynC@FPC mouse)

A SynC@FPC mouse (z178-4, 1415 s after A/C) walked toward a corner and abruptly entered behavioral arrest precisely when EEG γ-power declined sharply. EEG δ-power showed only a slight increase. Spindle waves appeared shortly after the onset of State-C in this case. The movie is shown in real time.

Movie S15. Treadmill running before i.p. A/C (SynC@FPC mouse)

A mirror beneath the treadmill captured normal running and transient stalling movements of the SynC@FPC mouse (z251-3, 1478 s before A/C), whose hindlimbs were widely spaced, providing stable treadmill control. The movie is shown in real time.

Movie S16. Treadmill running after i.p. A/C (SynC@FPC mouse)

The same SynC@FPC mouse (z251-3, 614 s after A/C) as in Movie 15 showed somewhat clumsier running (hindlimbs narrowly spaced) and occasional stalling, failing to adequately control the treadmill. The movie is shown in real time.